Algorithms for the Analysis of 3D Magnetic Resonance Angiography Images

Xavier Tizon

Centre for Image Analysis
Uppsala

Doctoral Thesis
Swedish University of Agricultural Sciences
Uppsala 2004

Acta Universitatis Agriculturae Sueciae
Silvestria 316

ISSN 1401-6230
ISBN 91-576-6700-4

Printed at the Uppsala University Printing and Media Office 2004

Abstract

Xavier Tizon. *Algorithms for the Analysis of 3D Magnetic Resonance Angiography Images*. Doctoral Thesis

ISSN 1401-6230, ISBN 91-576-6700-4

Atherosclerosis is a disease of the arterial wall, progressively impairing blood flow as it spreads throughout the body. The heart attacks and strokes that result of this condition cause more deaths than cancer in industrial countries. Angiography refers to the group of imaging techniques used through the diagnosis, treatment planning and follow-up of atherosclerosis. In recent years, Magnetic Resonance Angiography (MRA) has shown promising abilities to supplant conventional, invasive, X-ray-based angiography. In order to fully benefit from this modality, there is a need for more objective and reproducible methods.

This thesis shows, in two applications, how computerized image analysis can help define and implement these methods. First, by using segmentation to improve visualization of blood-pool contrast enhanced (CE)-MRA, with an additional application in coronary Computerized Tomographic Angiography. We show that, using a limited amount of user interaction and an algorithmic framework borrowed from graph theory and fuzzy logic theory, we can simplify the display of complex 3D structures like vessels. Second, by proposing a methodology to analyze the geometry of arteries in whole-body CE-MRA. The vessel centreline is extracted, and geometrical properties of this 3D curve are measured, to improve interpretation of the angiograms. It represents a more global approach than the conventional evaluation of atherosclerosis, as a first step towards screening for vascular diseases.

We have developed the methods presented in this thesis with clinical practice in mind. However, they have the potential to be useful to other applications of computerized image analysis.

Keywords: Contrast-Enhanced Magnetic Resonance Angiography, Computerized Tomographic Angiography, blood-pool agents, segmentation, fuzzy connectedness, fast marching, vesselness, atherosclerosis, shortest path, vascular analysis, Maximum Intensity Projection, curvature, torsion

Author's address: Centre for Image Analysis, Lägerhyddsvägen 3, 752 37 Uppsala, Sweden

There are always alternatives.

Mr Spock, *The Galileo Seven*, stardate 2822.3

Contents

Algorithms for the Analysis of 3D Magnetic Resonance Angiography Images

Papers I – VI

Papers appended to the thesis

The thesis is based on the following articles, which will be referred to in the text by their Roman numerals.

I X. Tizon and Ö. Smedby. Segmentation with Grayscale Connectedness Can Separate Arteries and Veins in MRA; *Journal of Magnetic Resonance Imaging*, 15(4):438–45, 2002.

II A. Löfving, X. Tizon, A. Persson, and Ö. Smedby. Angiographic Visualization of the Coronary Arteries in Computed Tomography Angiography with Virtual Contrast Injection; *to be submitted for journal publication, pending the addition of new patient material.*

III E. Vidholm, X. Tizon, I. Nyström, and E. Bengtsson. Haptic Guided Seeding of MRA Images for Semi-Automatic Segmentation; *Proceedings of the 2004 IEEE International Symposium on Biomedical Imaging: From Nano to Macro, Arlington, VA, USA, 15-18 April 2004, pages 288–291.*

IV J. Kullberg, H. Frimmel, X. Tizon, L. Johansson, and H. Ahlström. Compensation for Geometrical Hardware-Induced Distortion in Contrast Enhanced Whole-Body Magnetic Resonance Angiography; *augmented version of an abstract submitted to ESMRMB 2004. To be submitted for journal publication.*

V X. Tizon, Q. Lin, T. Hansen, H. Frimmel, G. Borgefors, L. Johansson, and H. Ahlström. Identification of the Main Arterial Branches in Whole-Body Contrast-Enhanced MRA in Elderly Subjects Using Limited User Interaction and Fast Marching; *submitted for journal publication.*

VI X. Tizon, H. Frimmel, L. Johansson, and H. Ahlström. Objective Assessment of Vessel Geometry in 3D Whole-Body Contrast-Enhanced MRA; *to be submitted for journal publication.*

All papers published, in press or accepted for publication are reproduced with permission from their publisher. The author has significantly contributed to the work performed in all the papers. Development and testing of the algorithms was achieved for papers I, II, V and VI as well as clinical data processing for papers I, V and VI. The author participated in the elaboration of the methods described in paper II, IV and V, and more significantly in paper VI. The author also contributed to the writing of papers II, III and IV, and wrote most of the text of papers I, V and VI.

Faculty opponent is Dr. Grégoire Malandain, INRIA, Sophia-Antipolis, France.

List of abbreviations

API: Application Programming Interface
BP: Blood Pool
CE-MRA: Contrast-Enhanced Magnetic Resonance Angiography
CPR: Curved Planar Reformation
CTA: Computed Tomographic Angiography
DOF: Degree of Freedom
DSA: Digital Subtraction Angiography
ECG: Electro-Cardiogram
EDT: Euclidean Distance Transform
FM: Fast Marching
FOV: Field of View
GC: Grayscale Connectedness
GUI: Graphical User Interface
MIP: Maximum Intensity Projection
MPR: Multi-Planar Reconstruction
MRA: Magnetic Resonance Angiography
MRI: Magnetic Resonance Imaging
NMR: Nuclear Magnetic Resonance
PC: Phase Contrast (or Personal Computer)
PD: Proton Density
PDE: Partial Differential Equation
RF: Radio Frequency
ROI: Region of Interest
SNR: Signal to Noise Ratio
SR: Surface Rendering
TE: Time to Echo
TOF: Time of Flight
TR: Time to Repetition
US: Ultrasound
VR(T): Volume Rendering (Technique)

1 Introduction

Cardio-vascular diseases are the leading cause of death in western countries. Among them, atherosclerosis accounts for more than 70% of this mortality, alone responsible for more deaths than cancer. Atherosclerosis is a systemic disease of the vessel wall that evolves slowly over the years, often without any symptomatic manifestation. Yet, when it strikes, it can be dramatic, with plaque rupture and thrombosis causing unstable angina, myocardial infarction or sudden death. That is why it is crucial to develop methods to diagnose and evaluate risks associated with atherogenesis.

Medical imaging has emerged in the last two decades as an essential tool in clinical diagnosis and follow-up. As the technique evolves, the number of available modalities increases steadily, offering new ways to explore pathologies. But the complexity of images grows along with their quantity: three-dimensional, high-resolution datasets are becoming standard. Their correct interpretation requires highly trained experts and advanced technical equipment. This thesis aims at showing that this interpretation task can be made easier by the use of computerized image analysis and proper visualization techniques.

The datasets used in this thesis all come from emerging angiographic modalities:

- Blood-pool contrast-enhanced magnetic resonance angiography
- Coronary contrast-enhanced computerized tomographic angiography
- Whole-body contrast-enhanced magnetic resonance angiography

To improve the analysis and visualization of these datasets, we use in this thesis methods from:

- Fuzzy set theory and digital geometry
- Computer graphics
- Mathematical image analysis: partial differential equation, differential geometry
- Scale-space theory

The thesis is organized as follows. Section 2 focuses on the data themselves. It provides the reader with an overview of the medical context behind the image analysis projects. First with a brief introduction to atherosclerosis, and then to the physical and clinical aspects of Magnetic Resonance Imaging (MRI) and Angiography (MRA), including ways to visualize the acquired data. Section 3 introduces most of the mathematics behind the algorithms used to analyze angiographic images. First, the notion of connectedness is defined for grayscale images, and we show how to use it to segment arteries from veins. Then we introduce the shortest path problem and an algorithm to solve it in the context of vessel detection. The last part shows how the geometry of 3D curves can be measured to detect early signs of plaque vulnerability. Research not only consists in the introduction of new concepts, but also in their proper implementation [18]. Section 4 gives information about the way the new algorithms were implemented. Section 5 offers some views of the future, suggesting ways to improve our results and new research tracks. In section 6, we summarize the main results of the different articles included in this thesis.

2 Background

Our research has been articulated around two projects, involving different imaging protocols and image analysis methods. This section aims at presenting the background knowledge necessary to understand the papers included in this thesis.

2.1 Atherosclerosis

Diseases of the circulatory system account for nearly half of the deaths in western countries. Atherosclerosis belongs to this group, and will most likely be the principle cause of worldwide morbidity and mortality in the near future [126].

As early as 1740, Krell, a German physician, described calcic structures inside the arterial wall, which he named "bony plaque". Lobstein, nearly 100 years later, named the disease "atherosclerosis" [55]. The word atherosclerosis comes from the Greek words "athero", meaning gruel or paste, and "sclerosis", meaning hardness. It is a systemic disease: it affects the whole body. It is characterized by a local thickening of the innermost vessel wall layer, the intima (see Fig. 1), leading to a progressive reduction of the diameter of the arteries [3, 10, 102].

Atherosclerotic lesions, commonly called atheromas or plaque, are composed of accumulated intracellular and extracellular lipids, smooth muscle cells, and connective tissue. They can be found in any medium or large artery, but will most likely be near bifurcations and in highly curved vessels [145]. In order of frequency [86], they can be found in (see Fig. 2 and 3 for an anatomic chart of the main arteries):

- the abdominal aorta
- the coronary arteries, especially the proximal segments
- the arteries to and in the lower limbs: iliac, femoral, popliteal and tibial arteries
- the carotid, brachial, and vertebral arteries

The formation of atherosclerotic plaque is thought to be a continuous process, which may go on for several years without any symptoms. The detailed mechanisms of atherogenesis are still uncertain, and Stary suggested in 1994 a decomposition in eight different stages [148]. Stages 1 to 3 represent the progressive plaque buildup. They happen during childhood and young adulthood. The intima thickens as it slowly incorporates muscle cells, lipids and blood cells. At stages 4 and 5, the plaque is almost fully grown, but does not yet induce any symptom. The thickening of the plaque is accompanied by a compensatory dilation of the vessel, called arterial remodeling [49, 69, 166]. This way, a relatively large plaque may exist in the

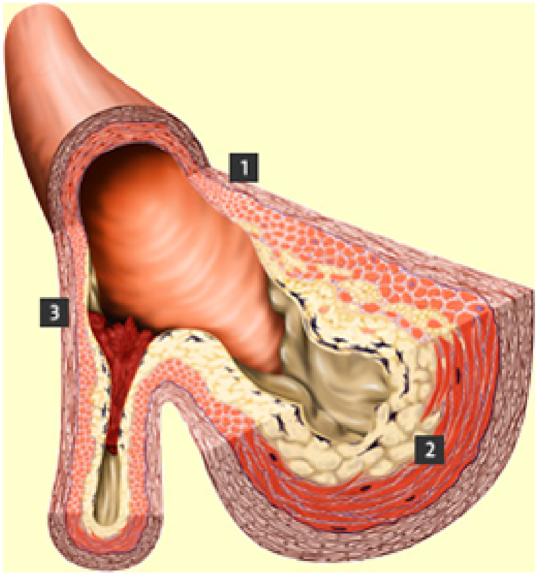

Figure 1: The artery wall consists of three layers: (3) a layer of connective tissue, the tunica adventitia; (1) a second layer of smooth muscle cells and elastic connective tissue, the tunica media; and a third layer of endothelial cells, the tunica intima. The central, blood containing space, is the lumen. Fatty deposits in the intima constitute the atherosclerotic plaque (2).
© Copyright Bayer HealthCare AG, Leverkusen, Germany.

arterial wall without any reduction in blood flow. Eventually, at stages 6 to 8, the large plaque may cause a diminished luminal diameter with consequent impairment of blood flow. To some extent, the body will protect itself by forming new blood vessels around the affected area. This is called developing “collaterals”. If the flow is reduced in the coronary arteries or in the large arteries of the legs, the patient may experience pain as angina or claudication. However, in many cases, the plaque does not give any notice until it ruptures. The rupture induces a thrombus formation with subsequent temporary or permanent occlusion of the vessel. In the coronary arteries, the result is a myocardial infarction, and in the arteries of the legs acute critical ischemia. Strokes and transitory ischemic attacks of the brain are often caused by thrombus formation on lesions in the carotid arteries.

Several risk factors have been identified [99]. Their relative importance is still a matter of active research:

- High Low Density Lipids cholesterol level
- Hypertension
- Tobacco smoking
- Diabetes
- Obesity
- Physical inactivity
- Genetic factors

Two strategies are possible for treatment, depending on the gravity of the disease. The medical approach includes a low-fat diet together with exercise, to lower blood lipid levels, lose weight, and to help develop collaterals. Medications are also useful: anti-platelets and anti-coagulants, to reduce the risk of clot formation in the vessels. When the disease has reached a certain stage, evaluated by clinical symptoms and the state of the vascular bed surrounding lesions, surgery is required to bypass or unblock the heavily stenosed arteries. Several techniques are available, which all require, in order to plan and evaluate the results of the procedure, a quantitative knowledge of vessel geometry.

Aging, atherosclerosis and vessel morphology. Recently the view that atherosclerosis only amounts to a matter of “plumbing” has been challenged [51, 87]. The role of inflammation in the process of atherogenesis has been recognized, and plaque can be seen as the scar tissue left by the inflammatory process. As such, its effects are very similar to those of aging. It is actually often mentioned that atherosclerosis may be viewed as an accelerated form of aging [41]. The effects of atherosclerosis can be observed locally, with a luminal diameter reduction, leading to stenosis and eventually

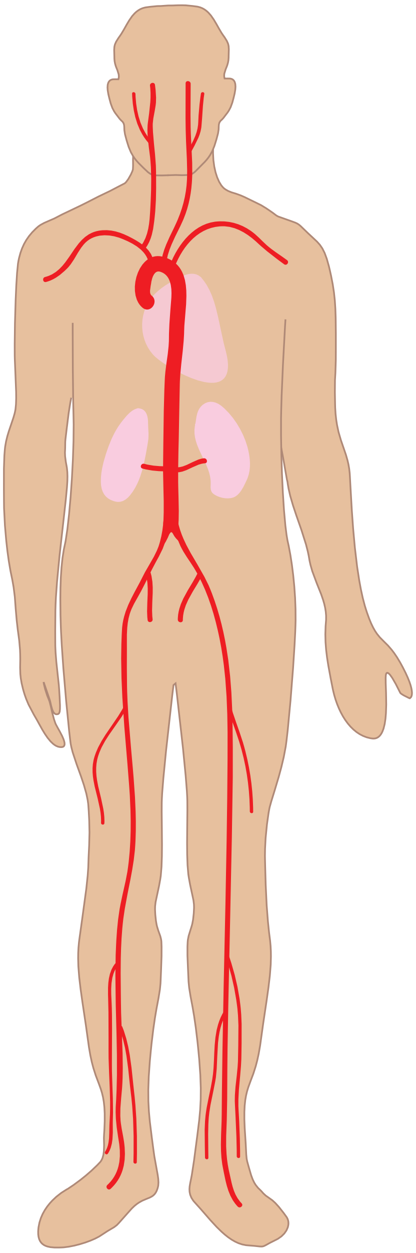

Figure 2: Schematic representation of the main arteries in the human body.

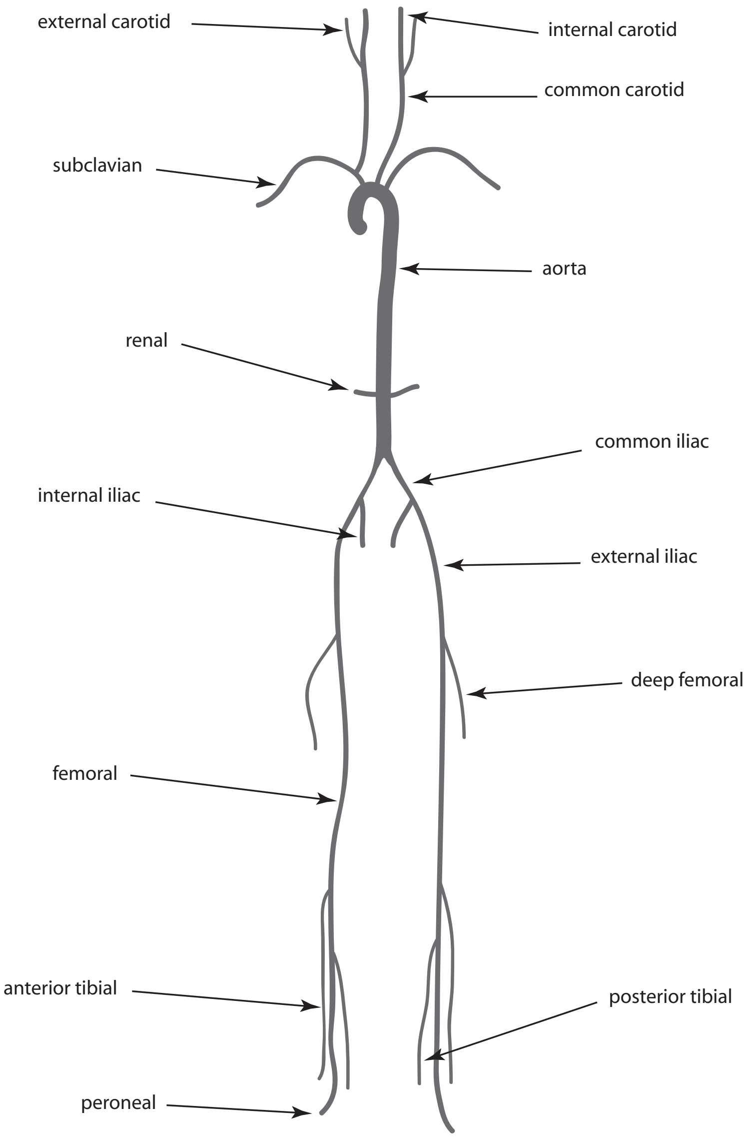

Figure 3: Name of the main arteries in the human body.

occlusion. But, as shown by recent research, the more global consequences may be even more critical to identify and measure. The whole vascular system reacts actively to the process of atherogenesis: the role of vasculature in atherogenesis is not simply a passive housing of atherosclerotic lesions. On the contrary, the vascular morphology evolves along with atherosclerosis progression in a process called arterial remodeling [69, 166]. The vessel wall gets stiffer as it loses its elasticity, and the outer arterial diameter increases as plaque grows within the lumen. This compensatory mechanism makes vessels longer, and thus more tortuous. With this new model, it is apparent that we need to target the underlying atherosclerotic vascular disease process instead of addressing the size of the lumen. The purpose of paper VI is to suggest a set of objective measures of the morphology of the main arteries in whole-body CE-MRA.

2.2 Data acquisition

2.2.1 Magnetic Resonance Imaging

The following sections present a brief introduction to the Magnetic Resonance phenomenon, and the way images are created from the MR signal. To get a more in-depth description of MRI, the reader is referred to [11, 38, 127] for example, and to [54] for the authoritative reference on MRI.

History. Nuclear Magnetic Resonance (NMR) was discovered independently by Bloch [13] at Stanford University, and Purcell [123] at Harvard. MRI was known as NMR until the “nuclear” connotation became unpopular, but both names denote the MR principle involved. In 1946, Bloch and Purcell found that when certain nuclei were placed in a strong magnetic field, they could absorb energy in the radio-frequency range, and re-emit this energy during the transition to their original state [127]. They were awarded the Nobel prize in physics in 1952 for their research. Spectroscopy remained the only application for many years, and R.R. Ernst received the Nobel prize in chemistry in 1991 for his work on NMR spectroscopy. It took 20 years and the work by Damadian [29], Lauterbur [83] and Mansfield [100], together with the introduction of the use of Fourier Transform in 1975 by Kumar [80], to produce images from the MR phenomenon. Lauterbur and Mansfield were awarded the Nobel prize in medicine in 2003 for “their discoveries concerning Magnetic Resonance Imaging”. Two other Nobel prizes have been rewarded for research in Magnetic Resonance: in 1944 in Physics to I. Rabi and in 2002 in Chemistry to K. Wüthrich.

Spin and precession. Some nuclei possess an intrinsic quantum property, the spin angular momentum $\boldsymbol{I}$. In the case of the ^{1}H hydrogen nucleus (the proton), it will give rise to a magnetic moment $\boldsymbol{\mu}$, which produces magnetic interactions with its environment :

$$\boldsymbol{\mu} = \gamma \boldsymbol{I} \quad , \tag{2.1}$$

where γ is the gyromagnetic ratio, uniquely defined for a nuclear isotope possessing a spin. So, a proton acts as if it were a spinning sphere of charge and mass, with an angular momentum $\boldsymbol{\mu}$. When placed in an external magnetic field $\boldsymbol{B}$, protons experience a torque $\boldsymbol{\Gamma}$, to align the moment with $\boldsymbol{B}$:

$$\boldsymbol{\Gamma} = \boldsymbol{\mu} \times \boldsymbol{B} \quad , \tag{2.2}$$

where × represents the vector cross product. Because of the angular momentum, the result is a precession of the proton around $\boldsymbol{B}$ at angular frequency ω_L, the Larmor frequency:

$$\omega_L = \gamma B \quad . \tag{2.3}$$

Only nuclei with non-zero magnetic moment can undergo NMR. Such nuclei must have an odd number of protons or neutrons (e.g. ^{1}H, ^{2}H, ^{13}C, ^{15}N, ^{31}P, ^{19}F). The magnetic moments $\boldsymbol{\mu}_i$ of the individual nuclei sum up to $\boldsymbol{M}$, the net magnetization vector:

$$\boldsymbol{M} = \frac{1}{V} \sum_i \boldsymbol{\mu_i} \quad , \tag{2.4}$$

where V is the total volume of the nuclei.

Excitation and relaxation. $\boldsymbol{M}$ has a component M_z along the z axis, which is conventionally chosen to point in the direction of $\boldsymbol{B}$, and a transverse component $M_\perp$. It is the transverse component of the magnetization vector that can be measured, using an antenna: this is the NMR signal. By induction, $M_\perp$ will produce a measurable current in the antenna. Inversely, if we generate a current in the antenna at the resonance frequency, it will cause $M_\perp$ to grow, as the nuclei are given energy and “tipped off” from their equilibrium position. The angle measuring how much energy they are given is called the *flip angle*.

The process of sending a pulse to excite the nuclei, and to measure the way they return to equilibrium with the same mechanism, forms the basis of NMR. The pulse has an energy in the radio-frequency (RF) range, to obtain resonance with the nuclei precessing at Larmor frequency. It is thus called a RF pulse.

The relaxation of the spins after excitation are governed by two physical processes:

- spin-lattice relaxation, with time constant T_1
- spin-spin relaxation, with time constant T_2

The Bloch equation describes the interaction of nuclear spins with the external magnetic field $\boldsymbol{B}$ and their local environment:

$$\frac{\partial \boldsymbol{M}}{\partial t} = \gamma \boldsymbol{M}(t) \times \boldsymbol{B} + \frac{M_0 - M_z(t)}{T_1}\boldsymbol{z} - \frac{1}{T_2}\boldsymbol{M}_\perp(t) \ \ , \tag{2.5}$$

where M_0 is the equilibrium sample magnetization, and $\boldsymbol{M}_\perp = [M_x, M_y, 0]$.

Solving the Bloch equation with a constant $\boldsymbol{B}$ and a RF pulse of 90° flip angle gives:

$$\begin{aligned} M_z(t) &= M_0\,(1 - e^{-t/T_1}) \\ M_\perp(t) &= M_0\,e^{-t/T_2} \ \ . \end{aligned} \tag{2.6}$$

This is the gradient echo experiment, the simplest MR sequence. It gives an easy interpretation for the time constants T_1 and T_2. T_1 is the time constant characteristic for the return of M_z to its equilibrium value M_0, and T_2 describes the way the transverse magnetization $M_\perp$ decays back to zero. These equations explain how contrast is built from the MR signal, by showing the link between the measured signal (M_z and $M_\perp$) and the local properties of tissue (T_1 and T_2).

MR Imaging. The process as it has been described up to now only gives one signal for the whole sample.To be able to do MR imaging, we need a way to localize the origin of the signal. This is done with the help of so-called *field gradients*. A field gradient is a spatially varying magnetic field added to the main field B_0. The field strength produced this way will be different for different spatial locations, and thus the resonant frequency ω_L of the nuclei will also depend on their location:

$$\omega_L(z) = \gamma(B_0 + zG_z) \ \ . \tag{2.7}$$

Applying a gradient along the z direction is called “slice selection”. If an RF pulse is applied to the sample when the gradient is active, only a thin slice of the volume will enter the resonant stage. The thickness of the slice will depend on (see Fig. 4):

- the slope of the gradient along z,
- the “RF bandwidth”, that is the spread of the RF pulse around its center frequency.

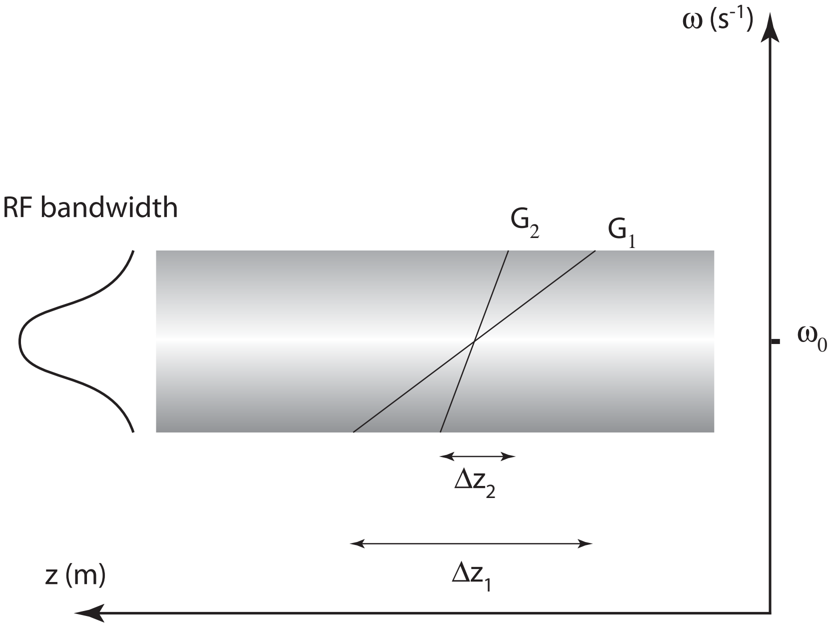

Figure 4: Slice thickness depends on gradient slope and RF bandwidth. G represents the gradient slope, and Δz the corresponding slice thickness.

Additional gradients along x and y allow for the complete spatial encoding of the MR signal. In practice, thin and well-defined slice excitation is difficult to achieve within system constraints and therefore spatial resolution along the slice-select direction[1] is typically less (3 mm) than the in-plane resolution (1 mm). The imaging equation gives the measured signal:

$$S(t) = \iiint \rho(x,y,z) e^{-i2\pi(xk_x+yk_y+zk_z)}\,\mathrm{d}x\,\mathrm{d}y\,\mathrm{d}z \quad , \tag{2.8}$$

where

$$k_x(t) = \gamma \int_0^t G_x(u)\,\mathrm{d}u \quad ,$$

and k_y and k_z are defined accordingly. The zero in the lower limit of the integral defining k_x represents the time at which the gradient is switched on. $\rho(x,y,z)$ is the density of protons in the sample. All integration limits are determined by the regions of non-zero spin density. Some terms of the imaging equation will depend on the type and the order of the applied RF pulses, the so-called imaging sequence. However, the signal is always proportional to the Fourier Transform of the proton density. As can be seen from the imaging equation 2.8, the signal is complex in the most general case. It is acquired in the Fourier domain, usually named k-space in MRI. An inverse Fourier Transform is then necessary to reconstruct the image from the MR signal. Two additional parameters are important to describe the imaging sequence:

- T_R, the time to repetition. It is the time interval between RF pulses.
- T_E, the time to echo. It is the time after the excitation pulse when the transverse magnetization is measured.

As an illustration of the effect of T_R and T_E, Fig. 5 shows the different kinds of contrast MRI can provide. For a particular imaging sequence, the "spin-echo" sequence, we have:

$$signal \propto \rho(1 - e^{-T_R/T_1}) e^{-T_E/T_2} \quad . \tag{2.9}$$

Therefore, the tuning of T_R and T_E allows the contrast to be built from different physical properties of the tissue.

2.2.2 MR artifacts

MRI is a very elaborate technique. Many things can go wrong when performing an MR examination. The defects that can be seen in an image depend on the scanner hardware, the imaging sequence, and even the subject inside the scanner. These defects are called artifacts, and we will describe some of them, relevant to our study, as they can be useful to understand the task at hand.

---

[1] Usually this is the axis of the scanner, which we will refer to as the z-axis.

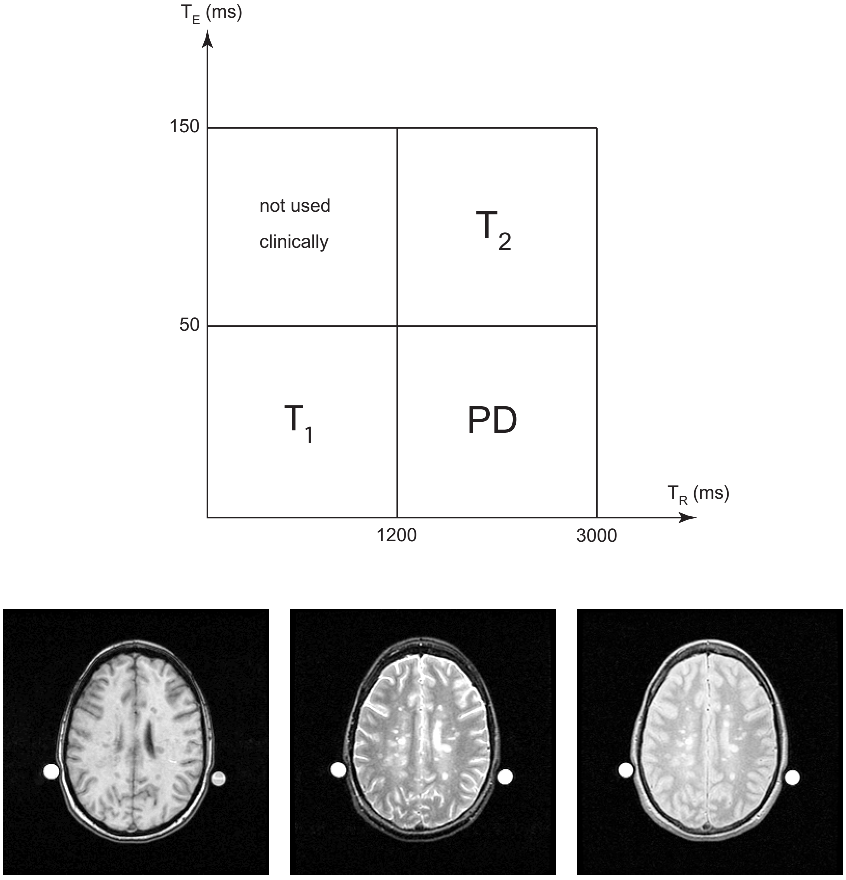

(a) T1-weighted (b) T2-weighted (c) PD-weighted

Figure 5: Upper row: typical values of T_R and T_E to build the three simplest kinds of contrast in MRI: signal weighted by T_1, T_2 and Proton Density (PD). Lower row: three axial slices of a human brain MRI scan, showing T_1, T_2 and PD-weighted contrast. We can clearly see the different information provided by the three modalities. The white disks on each side of the head are fiducial markers used to align the three images. The patient has multiple sclerosis, and lesions of the white matter can be seen as bright spots on the T_2 and PD images, and dark spots on the T_1 image.

Noise. The noise present in the MRI image is primarily due to thermal noises in the patient [110]. Noise present in the raw, complex MR signal acquired in the Fourier domain presents a Gaussian distribution. But the transformation to a magnitude image changes the Gaussian distribution of the data to a Rician distribution [143]. Noise mainly depends on:

- voxel size
- acquisition time
- main magnetic field intensity

At high Signal to Noise Ratios (SNR), the Rician distribution is very close to a Gaussian. Thus the assumption of Gaussian distributed noise is sound for the images we will work with.

Partial Volume Effect. A voxel actually contains many protons and the signal is averaged over the whole voxel volume. When a voxel contains more than one tissue type, the signal contribution of this voxel is a mix of the signals from the different tissue types the voxel contains: this is the Partial Volume Effect. It is a common property of every imaging system and cannot stricto sensu be called an artefact. However, as it causes blurred boundaries and signal variations within a volume, it is an important effect that has to be taken into account by the image analysis process.

Motion artifacts. Motion can be periodic, as caused by blood flow, heart beat, or respiration; or random, as a consequence of patient movements. The motion of the entire object during the imaging sequence generally results in a blurring of the entire image with ghost images in the phase encoding direction. More often, movements of a small portion of the imaged object will result in a blurring of that small portion of the object in the image. This type of artifact will be mostly visible around the patient's heart. The nature of the artifact depends on the timing of the motion with respect to the acquisition.

Geometrical distortions. As shown in section 2.2.1, gradients are used in MRI to provide spatial localization of the MR signal. But, unlike the ideal case of Fig. 4 showing the gradient as a straight line, real gradients present linearity defects. These effects get larger as voxels are further away from the magnet's center. The result is an error in voxel localization, that can be observed in the image as local, non-linear distortions. Additionally, gradient fields, which depend on the coils' geometry, are usually specific to each MR scanner, making these distortions even more difficult to handle [81]. In the particular case of the whole-body MRA sequence (see section 2.2.3), the size of the Field of View (FOV) is greater than in conventional imaging, making distortions even more apparent (see an example in Fig. 6). The purpose of Paper III is to model these distortions using a phantom [165], to be able to correct their effects and thus improve the quality of subsequent volumetric quantitative measurements.

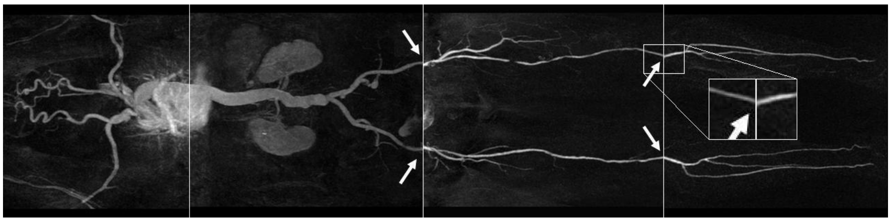

Figure 6: Geometrical distortions as they can be seen on a whole-body MRA volume. Vessels in the distal portion of the field of view are curved towards the image axis.

2.2.3 *Magnetic Resonance Angiography*

The first angiographic experiment dates back from early 1896 [56], just a few months after Roentgen discovered X-rays (see Fig. 7). Vessel visualization examinations entered clinical practice with the invention of Digital Subtraction Angiography (DSA) in the 1970s [79], which has become and still remains the gold standard for vascular studies. In DSA, a catheter is used to inject a radio-opaque contrast agent directly into the arteries. The catheterization is an intervention presenting the risk of severe complications. Moreover, the contrast medium, containing iodine, can cause serious side effects, such as allergy-like reactions or renal failure. See Fig. 8 for an example of a DSA image.

Ultrasound (US) [119], Computed Tomographic Angiography (CTA), and the more recent variant of DSA, 3D rotational angiography [141], are other techniques used to image vascular territories. Table 1 summarizes the main characteristics of the most widely available angiography modalities. As an alternative, MRA offers a procedure that is safe for the patient, with good spatial resolution, even if not matching that of DSA, and inherent 3D acquisition.

There exist three major techniques to perform angiography with MRI [76]:

- Time of Flight (TOF) [167]. It uses the fact that, as blood is circulating even during the acquisition, its magnetization properties differ from the surrounding, non-moving tissue. For optimal conditions, the image plane has to be oriented perpendicular to the main flow.

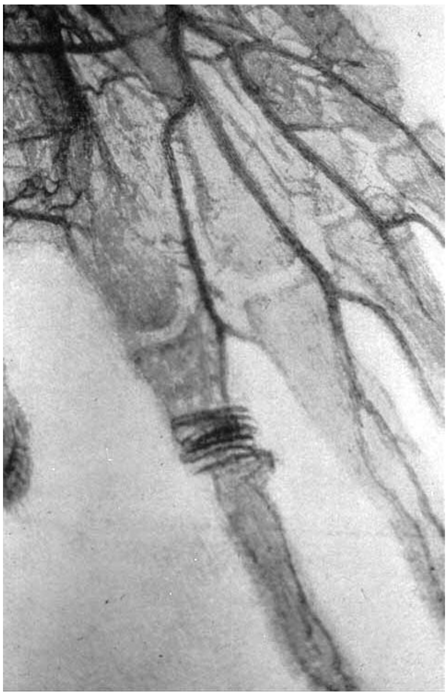

Figure 7: The very first angiographic image, 1896. E. Haschek and O. Lindenthal used bismuth, lead, and barium salts as contrast medium to perform the first X-Ray angiogram, using an amputated hand.

Figure 8: Example of a DSA image of the carotid artery, branching into the internal and external carotids. A stenosis can clearly be identified.

- Phase Contrast (PC) [163]. This technique is based on the linear relationship between the phase of moving spins and their velocity. The MR signal is directly related to blood flow velocity.
- Contrast-Enhanced (CE) [21, 28, 90, 101]. Like in DSA, contrast agents have been developed to be used in MRA. They are injected intravenously and reduce the T_1 relaxation time of the surrounding blood, making vessels appear brighter on T_1-weighted images. Often based on Gadolinium, they stay in the vascular bed for only a short period of time (minutes). It is important to note that, unlike DSA, MRA shows the effect of the contrast agent on proton relaxation around contrast molecules, and does not show the contrast agent itself. By timing the injection so that the contrast medium reaches the vessels of interest during image acquisition, it is possible to achieve exclusive arterial enhancement [33, 121]. The total volume of injected contrast medium is called the bolus, and the synchronization of injection and scan time is called *bolus chase*.

Flow-based techniques, like TOF-MRA and PC-MRA are of limited practical use. They require long acquisition times, and the quality of the images depend on the orientation of vessels and blood flow patterns. In addition, the size of the FOV is limited, and many parameters have to be set in order to obtain optimal results. CE-MRA is therefore the preferred technique in most vascular areas.

Blood-pool contrast agents. A new family of contrast agents has been developed recently [67, 82, 170], which are currently in the last phase of clinical trial, meaning that they are still only used on patients for research purposes. Rather than diffusing quickly through the vessel wall, Blood-Pool (BP) contrast agents remain intravascular much longer than conventional contrast agents (typically more than an hour). They can thus be used to produce images of the vascular structure during steady state, that is, when the whole vascular tree is filled with contrast. This presents both advantages and drawbacks:

☺ It allows for longer acquisition times, and significantly improves the Signal to Noise Ratio (SNR). It also allows new kinds of imaging techniques (e.g. whole-body imaging, perfusion studies in ischemic tissues, or studies of vascular modifications around and inside tumors).

☹ Arteries and veins are enhanced simultaneously. Since the two vessel types often run close to each other, they produce very intricate datasets that are difficult to interpret (see Fig. 9).

Table 1: Comparison of CE-MRA and other contrast based techniques [106]

	CE-MRA	**CTA**	**DSA**	**US**
Signal	magnetic pulse	X-Ray	X-Ray	sound wave
Contrast	e.g. Gadolinium	iodine based	iodine based	bubbles
Injection	intravenous	intravenous	intra-arterial	intravenous
Radiations risks	none (?)	large	significant	none
Other risks	contrast agent	contrast agent	bleeding, embolism, contrast agent, infection	small
Resolution	low (1 mm)	high	high (0.2-0.6 mm)	low
Remarks	contra-indications: metallic implants			bed-side

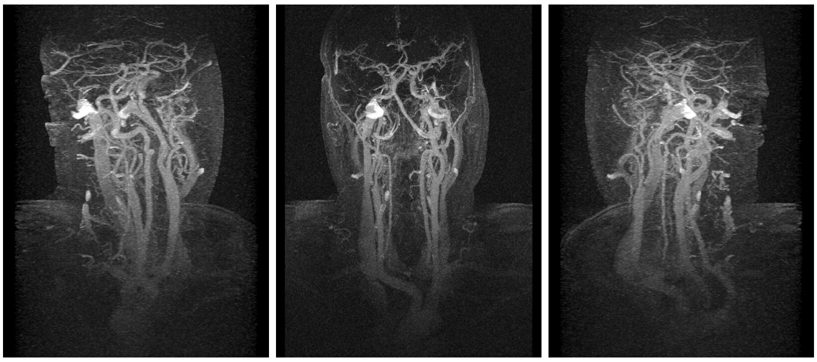

Figure 9: Maximum Intensity Projections (MIP) of a typical blood pool angiography data set, showing the vessels of the head and neck. Three MIPs are presented, with varying angles around the y (head to feet) axis: -45°, 0° and 45°.

In the diagnosis of atherosclerosis, arteries are the main objects of interest. The datasets produced by BP-CE-MRA have thus raised a problem, arteries-veins separation, which can be solved by, for example, using image processing techniques [14, 84, 103, 161, 162, 174]. The purpose of paper I is semi-automatic arteries-veins separation.

Whole-body CE-MRA. The systemic distribution of atherosclerosis requires the use of techniques which can assess the arterial system as exhaustively as possible. We describe here a technique for a whole-body MR angiographic examination of the atherosclerotic patient (see Fig. 10). This protocol was used to produce data for the studies of papers III to VI [52, 62, 130].

All imaging was performed on a 1.5 T Gyroscan NT (Philips Medical Systems, Best, the Netherlands) using MobiTrack software, the standard body coil and a specially built table top extender (see Fig. 11). A low-molecular Gadolinium-chelate was injected at a rate of 0.6 ml/s for 67 s, yielding a total volume of 40 ml. Breath holding was performed for the upper segment of the body, covering the carotid arteries and the thoracic aorta, as well as for the next segment, covering the abdominal aorta, renal arteries and aortic bifurcation. This is necessary to reduce motion artifacts caused by respiration to minimum. The sequence was a 3D RF-spoiled gradient echo with TR/TE/flip angle=2.6/1.0/30°. The matrix was 512×512 (pixel spacing 0.78 mm) and the FOV was $400 \times 400\,\mathrm{mm}^2$ with thirty 4 mm thick partitions, zero-filled and interpolated to 60 partitions of 2 mm by the scanner. This gives us rather big images, as the total size of a data volume for one patient is: 4 subvolumes $\times$ 512^2 in-plane pixels $\times$ 60 slices $\times$ 2 bytes of data by voxel $=$ 120 MB of raw data. An overlap of 3 cm between each station gave a maximum total length of coverage of 171 cm. The scan time for each station was 17 s. Including table top movements and instructions for breath-holding, the total scan time was 87 s. The most crucial parameter is timing: if the image is acquired too early after contrast injection, the vessels will not be visible, due to poor contrast filling. If, conversely, the operator waits too long before the acquisition, veins will be enhanced and will overlap arteries. The timing quality is one of the limiting factors for successful image analysis of MRA data.

2.3 Visualization of angiographic images

Because of the increasing size and complexity of medical datasets, it has become crucial to choose the right method to visualize 3D images on 2D screens. There exist many methods (see [66] for a review, and [70] for more in-depth details). This section briefly presents the ones that are useful to visualize angiographic data in a clinical setting.

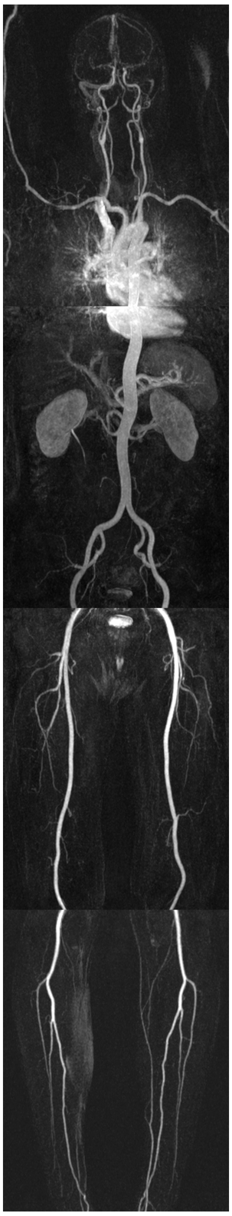

Figure 10: Example of a whole-body data set. The image is a concatenation of MIPs of the four sub-volumes produced by the imaging protocol. The four stations are, from top to down: supra-aortic arteries and thoracic aorta; abdominal aorta, renal arteries and iliac arteries; femoral and popliteal arteries; tibial and peroneal arteries, continued at varied length below the ankle.

Figure 11: Setup for a whole-body MRA examination. Patients are positioned supine (on their back), feet first. Their arms are raised on each side of their head, to avoid fold-over. Prior to the whole-body acquisition, a test scan is performed, to optimize the timing of contrast agent injection. During the acquisition, the table moves between the four stations.

2.3.1 Rendering of 3D data

Volume visualization aims at presenting 3D data on a 2D screen. Four volume visualization techniques have proven useful over the years for clinical angiographic practice [9]: Multi-Planar Reconstruction (MPR), Maximum Intensity Projection (MIP), Surface Rendering (SR) and Volume Rendering (VR).

Multi-Planar Reconstruction. This is a complicated term for a very simple method. From a 3D volume, 2D slices are shown on the screen. These slices are the intersections of the volume by planes, either orthogonal to the original acquisition frame, or oriented arbitrarily. In the latter case, interpolation of the original data is needed to produce the grayscale values of the intersected pixels. As MPR displays the original, possibly interpolated, graylevel values, it is always the visualization method that is the reference in case of doubt. It is also possible to display the intersection of the data volume with any surface [63, 122]: the technique is called Curved Planar Reformation (CPR). It is particularly useful in the context of angiography, where the intersecting surface can be chosen to include the centerline of the vessel of interest, thus showing a cut of the vessel lumen along the vessel course (see Fig. 12, from [64]). Pushed even further, the technique can produce visual renderings of the lumen of a whole arterial tree in one image [65].

MIP. Maximum Intensity Projection is the most common visualization technique aside from MPR. It shows, in a given direction, the maximum grayscale value along a ray that is shot in that direction intercepting the volume. When the direction does not coincide with the original volume frame, interpolation is needed to produce grayscale values along the ray. This makes it a rather expensive technique in terms of processing time. A considerable amount of research has been done to make it faster [108, 152, 178], using either dedicated hardware or smarter algorithms. A vast amount of enhancements of the MIP have also been proposed, as thin-slab, thick-slab, depth-coded MIP or local MIP [134]. MIP has the following advantages and drawbacks:

- ☺ It looks like a conventional, X-Ray angiogram. This is a non-negligible asset, as it allows experienced radiologists to interpret MIP images without additional training.
- ☺ The distribution of graylevels in the MIP is close to the one observed from the original volume.
- ☺ It is adapted to angiography, where the objects of interest are bright.
- ☹ The resemblance between MIPs and DSA might also be seen like a drawback, as the way grayscale values are integrated along the ray is not the same as for densitometric projections like DSA. In DSA, the displayed grayscale reflects the attenuation of the light source as it traverses the body, measures as the integral of the absorption function along the ray. In a MIP, information from only one voxel is displayed. A lack of knowledge from the physical process can lead to misinterpretation of the images.
- ☹ The depth information is lost on static MIPs.
- ☹ The vessel diameter is overestimated [5, 137].
- ☹ The Contrast to Noise Ratio (CNR) is decreased.

For all these reasons, it is recommended not to use static MIPs, but to gather MIPs from different projection angles. This can be done either by pre-computing MIPs for a given set of angles, or using a reasonably powerful workstation, displaying real-time dynamic MIP rendering with a free angle projection. See Fig. 13(a) for an example of MIP.

Surface Rendering. The principle of surface rendering is as follows. First the objects of interest must be identified in the slice images by segmentation. This is usually done by thresholding, resulting in a binary volume. The boundary of the binary volume is then approximated by a set of poly-

Figure 12: curved MPR of a CTA data set, for which the intersecting surface follows the main arteries of the peripheral vasculature. Reproduced with permission from [64].

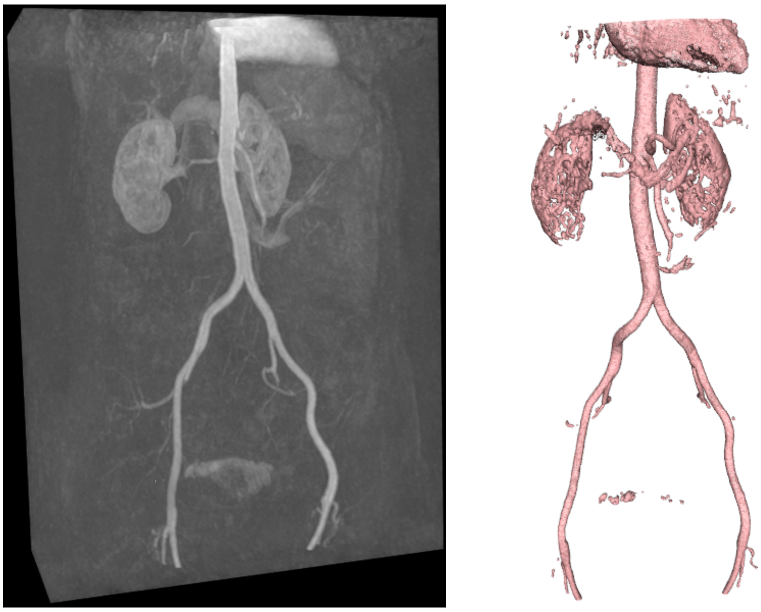

(a) MIP (b) Surface rendering

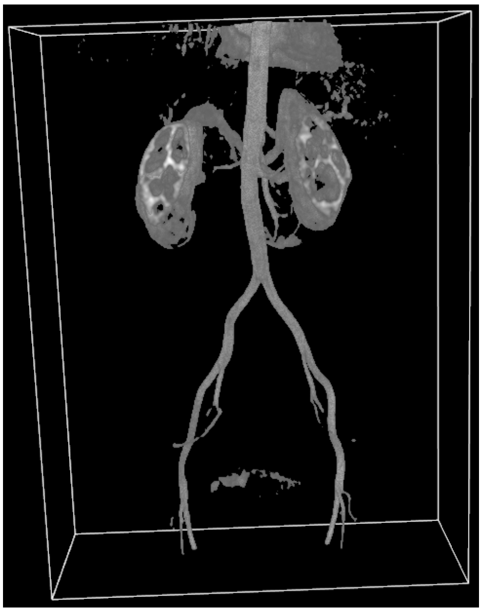

(c) Volume rendering

Figure 13: MIP, surface and volume rendering of the same data set.

gons. The most popular method to approximate the binary boundary is the Marching Cube Algorithm [97]. Virtual light is sent towards the object and is reflected on the facets, using a model of the interaction of the light ray and the surface. For the perception of the three-dimensional structure it is helpful if the viewpoint is dynamically moved. This is easily done in real time, due to the simplification in the data brought about by the polygon modeling step. See Fig. 13(b) for an example of surface rendering.

Volume Rendering. Volume rendering does not require any preliminary segmentation step. Each voxel is mapped via a transfer function to optical quantities such as color and opacity. Then a ray is sent from each pixel in the image plane through the volume data. As it passes the volume, each voxel it encounters may contribute to the pixel value, depending on its intensity and depending on the opacity of all voxels closer to the image plane. In the end, a pixel's intensity integrates contributions from many voxels along the ray. In nearly all applications, some part of this process involves the first order differential structure of the field: the gradient. More recently, higher order differential operators have been proposed [72, 136]. See Fig. 13(c) for an example of volume rendering.

2.3.2 Haptic rendering

When it comes to 3D visualization, the way the operator interacts with data is also important. The usual input devices that are available on any workstation are the mouse and keyboard. They are not adapted to the manipulation of 3D objects.

Haptic rendering with a PHANTOM input device is a possible candidate to provide better 3D interaction capabilities. It provides six degrees of freedom (3 rotations and 3 translations) together with a haptic feedback. It also provides three degrees of freedom for the haptic feedback, which is the output of the system (a 3D force vector). Figure 14 shows the setup of a haptic platform used to segment angiographic data in paper III. It is able to render angiographic volumes in real-time, which means 20 Hz for the stereo display, and 1 kHz for the haptic feedback.

Figure 14: The haptic desktop display. The PHANTOM device, a stylus that allows interaction with 6 degrees of freedom (3 rotations and 3 translations), is positioned beneath a semi-transparent mirror. The graphics are projected through the mirror to obtain co-location of graphics and haptics.

3 Vascular image analysis

The purpose of this section is to provide some background information about the image analysis methods used throughout the different applications in this thesis. For more thorough reviews on the analysis of vascular images, see [19, 40, 153, 154].

The methods will be described in three dimensions, as this corresponds to the data we have been working with. We will refer to our datasets as images, independently of their dimensionality, but most often they will be 3D. We call a scene a mapping $f : \mathbb{R}^3 \longrightarrow \mathbb{R}, \mathbf{x} = (x, y, z) \mapsto f(x, y, z)$. An image is an estimate of a scene, discretized and quantized on a finite grid [43]. It is represented by a 3D array of numbers $f = \{f[i_x, i_y, i_z]\}_{i_k=1,\ldots,N_k}$, provided the grid is a regular mesh. N_x, N_y and N_z are the dimensions of the image along the x, y and z directions. We will not assume an isotropic grid, unless stated otherwise. As is often the case with medical 3D data, most of the volumes we deal with have a resolution that is higher in-plane than between slices (see section 2.2.3 for the MRA case). A voxel v is denoted by its coordinates (x, y, z) and a grayscale value $f(v)$ in 3D. Each voxel has 26 "direct" neighbors in a $3\times3\times3$ neighborhood: 6 sharing a face, 12 sharing an edge, and 8 sharing a vertex. This 26-neighborhood defines the connectivity that will be used in the following (if not stated otherwise).

3.1 Grayscale connectedness

As mentioned in section 2.2.3, and as illustrated in Fig. 9, datasets produced with Blood Pool CE-MRA are very complex. In this section, we give the theoretical background necessary to introduce the segmentation method described in papers I and II, used to simplify the display of Blood Pool CE-MRA images.

As early as 1979, Rosenfeld suggested a generalization of the concept of connectedness to grayscale images [128]. In binary images, two voxels are connected, if they belong to the same connected component [50]. By analogy, it is possible to define a "degree of connectedness" that is an expression of the "hanging-togetherness" of two voxels within an image [158]. The concept was theoretically extended by Udupa in [113, 132], and found many applications to segmentation [31, 32, 112, 159]. The variant we present here is, to some extent, a simplification of the more general framework of Udupa, but its fast algorithmic implementation is original. It borrows ideas from the distance transform computation method called "chamfering" [15, 30]. In addition, it is also interesting to notice that this raster scan technique (also called "sweeping"), has found recent applications in the numerical resolution of Hamilton-Jacobi equations [104, 156, 168], which is a problem related to our work on Fast Marching (see section 3.2).

3.1.1 *Definition*

In a binary volume, two voxels are connected to each other if they belong to the same connected component, that is, if they are both, e.g., white, and there is a path joining them consisting only of white voxels. This concept can be generalized to grayscale images, yielding a "degree of connectedness", which values are not restricted to 0 and 1.

Let $\mathcal{N}(v)$ denote the 26-neighborhood of a given voxel v. A path ρ joining two voxels v and v' is a sequence of distinct points w_i :

$$v = w_0, w_1, \ldots w_{n-1}, w_n = v' \quad ,$$

such that for each $i, 0 \leq i \leq n-1, w_{i+1} \in \mathcal{N}(w_i)$. Following Rosenfeld's terminology [128, 129], the strength of a path (with respect to f) is the minimum of the intensity values of its constituents, i.e.

$$S_f(\rho) = \min_{w_i \in \rho} f(w_i) \quad . \tag{3.1}$$

The degree of connectedness between two voxels v and v' is defined as the maximum of the strengths among all possible paths joining v and v':

$$C_f(v, v') = \max_{\rho(v,v')} S_f(\rho) \quad . \tag{3.2}$$

Note that, for any voxel v, $C_f(v, v) = f(v)$.

Now let s be a fixed starting point, a so-called seed voxel, and S a set of seed voxels (not necessarily contiguous), defining a seed region. We define, for any voxel v in the 3D image,

$$C(S, v) = \max_{s \in S} C(s, v) \quad . \tag{3.3}$$

That is, the degree of connectedness between a voxel and a region is the maximum of the connectedness values for all the voxels in that region.

A rather serious limitation of this definition of connectedness is that it is only able to segment bright objects from each other. This comes from the fact that the strength of the path, in (3.1), is defined using only the intensity values. There are two possible generalizations of this:

- Instead of using the grayscale values from the original images to define grayscale connectedness, Udupa uses a dedicated affinity function [158]. This function measures the degree of resemblance between two voxels in the image. It is the most general formulation.

- Dellepiane [31] uses a relative and normalized version of the gray scale, in order to treat bright and dark objects equally.

However, the formulation of (3.1) is adequate to solve the problems described in papers I and II where bright objects have to be segmented from each other.

3.1.2 Algorithm

The "natural" way to compute the connectedness value for all voxels in the image would require finding all possible paths between all pairs of voxels. It is a computationally very demanding task, known as the "all-pairs shortest path problem". A possible solution, described in [26], has running time $\mathcal{O}(n^3)$ and uses a data structure of size n^2, where n is the number of voxels. These are rather drastic requirements when dealing with large images. However, considering the following observation, the whole computation is not necessary: if, for a voxel v, the values $C(S,w)$ are known for all neighbors $w \in \mathcal{N}(v)$, then the degree of connectedness $C(S,v)$ is the greatest connectedness value among the neighborhood of v, as long as it does not exceed the graylevel value of v, $g(v)$. This can be written:

$$C(S,v) = \min\{f(v); \max_{w \in \mathcal{N}(v)} C(S,w)\} \ . \tag{3.4}$$

This is a recursive definition of grayscale connectedness. It allows us to compute a 3D image in which each voxel has as its intensity the degree of connectedness to one given seed region: the "connectedness map". To achieve our goal of segmentation using the connectedness maps, we must compute as many connectedness maps as we have seed regions. Each voxel will then be assigned to the seed region it has the highest connectedness to.

Computing several connectedness maps is unpractical, and can be avoided by the use of an additional image that we call the label map. The segmentation process is equivalent to the propagation of label values from the seed points, using an algorithm that can be summarized by the pseudo-code in Algorithm 1, p. 49.

The computation scheme is based on a chamfer algorithm, similar to the one used to compute distance transforms [16]. The image is processed sequentially forward, from voxel $(1,1,1)$ to voxel $(x_{\max}, y_{\max}, z_{\max})$, and backward, then forward again, etc, until a stopping criterion is met. The criteria available in our implementation are the number of forward-backward iterations and the number of changes in the connectedness map between two iterations. During each iteration, computations are performed considering only a reduced neighborhood, as can be seen in Fig. 15.

The procedure is similar to the well-known region growing technique [177], such as the "magic wand" of most image processing pro-

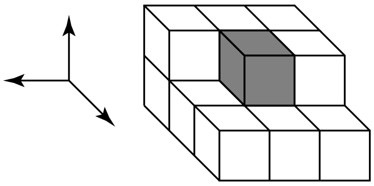

Figure 15: Neighborhood of the 13 previously visited voxels for a backward scan.

grams. But the usual formulation uses a similarity criterion based on the grayscale value to propagate [142]. Grayscale connectedness, using the connectedness value along a path as a propagation criterion, includes additional, topological, information. Additionally, the notion of competing seeds of different colors may provide a solution to the standard “leakage” behavior of region growing. See Fig. 16 for an illustration of the color propagation process, and Section 6.1 for some results.

3.2 Fast marching

In this section, we describe an algorithm that is used in papers V and VI to identify vessels of interest in whole-body angiograms. Our approach is to formulate the problem in terms of finding the shortest path, according to some metric, between two points in the MRA volume.

Finding the shortest path between two points in a given domain is a problem that arises, for example, in the context of differential geometry, where the shortest path is called a geodesic in the domain. Algorithms to compute this path have been studied within the field of graph theory. The simplest form of the problem is to consider the input domain as a finite graph, where weights are assigned to every arc linking two vertices. A shortest path between two vertices in the graph is the one with the lowest cumulative cost among all admissible paths. The most popular algorithm to compute this path is due to Dijkstra [36]. It solves a rather general form of the problem: to find the shortest path between a starting point and any other point in the domain. A more efficient variant is the so-called A* algorithm, which finds the shortest path between a starting point and an end point within a reduced search space. Both these algorithms extend the more basic method of breadth-first search, which is also useful in Image Analysis [144].

The common problem of graph-based approaches is that they suffer from a digitization bias [157], also called metrication error [25]. This means that

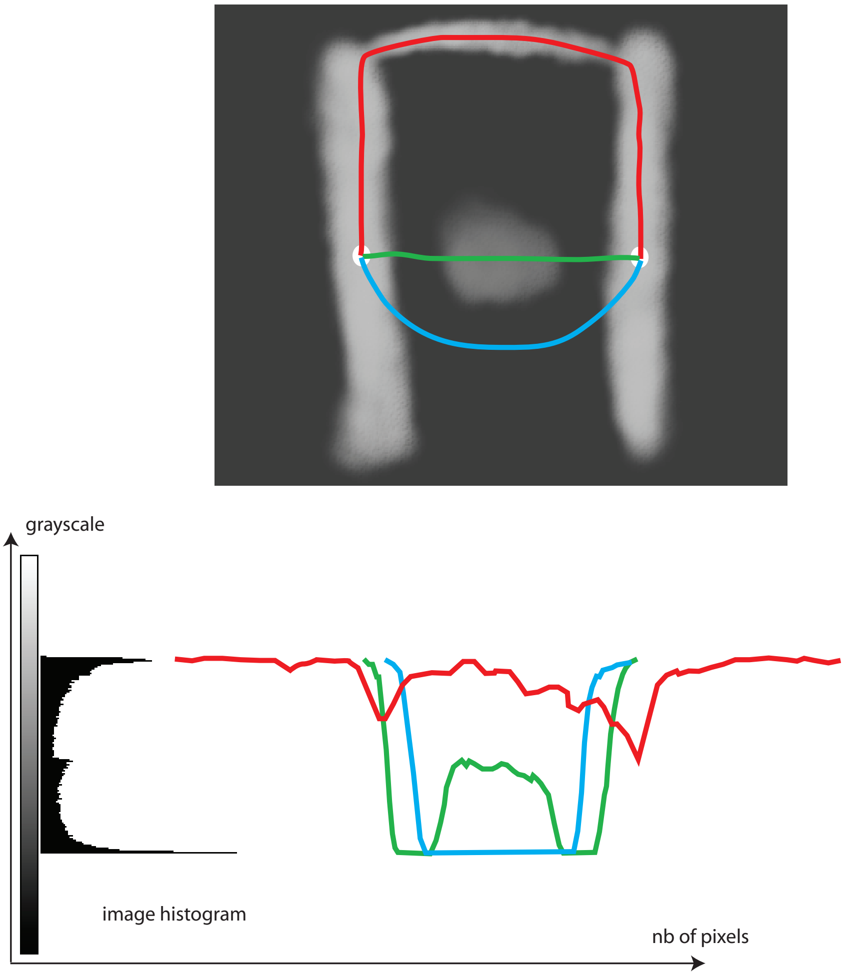

Figure 16: Illustration of the concept of grayscale connectedness. Three possible paths between two pixels in a synthetic image are represented. The graylevel values are also plotted against the pixels forming the path, in a so-called profile plot. The grayscale connectedness is the maximum grayscale value among all possible paths of the minimum along each path. In this example, grayscale connectedness will thus favor label propagation along the red path, as its minimum value is higher than for the blue or green paths.

the resulting path does not get closer to the euclidian path as the grid gets finer, a property also denoted as multigrid convergence [23]. The root of the problem is that on a graph, the set of allowed directions of motion is discretized very coarsely: only four directions are allowed. The motivation to choose a method that computes a path which is closer to the "ideal", euclidian path is exemplified in Fig. 17, adapted from Thomas Deschamps' PhD thesis [34].

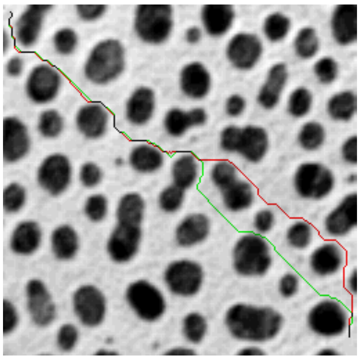

Figure 17: Comparison of shortest paths computed using Fast Marching and the Dijkstra algorithm. The image represents cells as viewed by a microscope. The values of the cost function are inversely proportional to grayscale image values. The light path is the Fast Marching path, whereas the dark path is found using Dijkstra's algorithm. One can clearly see that Dijkstra's algorithm is less prone to use diagonal steps, thus leading to different, longer paths. This comes from the fact that the Dijkstra algorithm implicitly uses the $L1$-norm to compute distances between pixels, whereas fast marching uses the more correct L_2, Euclidean norm.

The more recent emergence of minimum-cost path problems in the context of Image Analysis has brought the idea that they could be considered as the discretization of an underlying continuous problem. Let F be a positive function defined in $\mathbb{R}^3$: the cost function. Given points A and B, we wish to find the path Γ that minimizes the cumulative cost in going from A to B. That is, if $\gamma(s)$ is the arc length parametrization of Γ, we wish to minimize the integral

$$\int_{A=\gamma(0)}^{B=\gamma(L)} F(\gamma(s))\,\mathrm{d}s \quad , \tag{3.5}$$

where L is the length of Γ. We define a function $u(\mathbf{x})$ that is the minimum cost to go from A to any $\mathbf{x} \in \mathbb{R}^3$

$$u(\mathbf{x}) = \min_{\gamma} \int_A^{\mathbf{x}} F(\gamma(s))\,\mathrm{d}s \ . \tag{3.6}$$

The level set $u(\mathbf{x}) = c$ is the set of points that can be reached with the same minimum cost c. The level sets form closed surfaces in $\mathbb{R}^3$, perpendicular to minimum cost paths. By studying the evolution of these level sets, we can formulate a dual interpretation of the problem in terms of front propagation. The level sets of u grow away from A (as F is always positive), at a speed that depends on the values of F. This formulation is actually more general, and is the starting point of Level Set methods [4, 140]. With this formulation, the value of u can be interpreted as an "arrival time" of the front, and the cost function as a speed term of the front.

Differentiating the expression for u, we see that $\nabla u(\mathbf{x}) = F(\mathbf{x})\boldsymbol{n}$, where $\boldsymbol{n}$ is a unit vector, normal to the level set at $\mathbf{x}$. Then u satisfies the following boundary condition problem, known as the *eikonal equation*:

$$\begin{cases} \|\nabla u(\mathbf{x})\| = F(\mathbf{x}) \\ u(A) = 0 \end{cases} \ . \tag{3.7}$$

Once we have solved 3.7 for u, we can find the minimum cost path by following ∇u from B back to A. That is, we solve

$$X_t = \nabla u, \quad X(0) = B \ , \tag{3.8}$$

until we reach A. This is called back-propagation (see Fig. 18). Equation (3.8) is an ordinary differential equation, that can be solved in an efficient and correct way using a gradient following method, such as the Runge-Kutta method [120].

In 1995, Tsitsiklis and Sethian independently introduced an efficient method to compute discrete solutions to the eikonal equation (3.7) [4, 157], based on upwind schemes to approximate the gradient, and a Dijkstra-like algorithm. These two components will be described in more detail in the following two sections.

3.2.1 Gradient approximation

The classical gradient approximations, using for example centered differences, are not suited to solve (3.7), and produce instabilities in the solutions [140, pp. 41–43]. More advanced approximation schemes are needed, like the ones developed to compute solutions of a more general class of Partial Differential Equations: the static Hamilton-Jacobi equation [115]. The

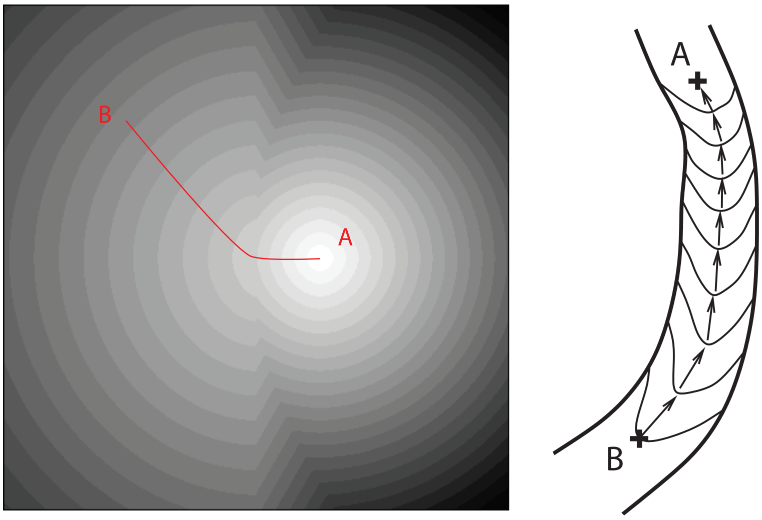

(a) Shortest path (b) Back propagation

Figure 18: (a) Example of a shortest path computation. The image is divided into two subparts. The left half of the cost image (not shown here) has constant value of 100, and the right half a constant value of 200. It is then “more costly” to travel in the right half. The graylevel disks represent the points of equal arrival time when starting from point A. The shortest path joining B to A is always perpendicular to the isophotes in the “arrival time” image shown here. This image actually allows to compute the shortest path between any point in the image and the start point A. (b) Back propagation from the end point B to the start point A, by following the gradient of the fast marching result.

first-order discretization scheme we use is [138, 139]

$$\begin{aligned}\|\nabla u(x,y,z)\|^2 \simeq \quad & \max(D^{-x}u, -D^{+x}u, 0)^2 \\ & + \max(D^{-y}u, -D^{+y}u, 0)^2 \\ & + \max(D^{-z}u, -D^{+z}u, 0)^2 \quad ,\end{aligned} \tag{3.9}$$

where

$$D^{-x}u = \frac{u_{i,j,k} - u_{i-1,j,k}}{\Delta x} \qquad \text{and} \qquad D^{+x}u = \frac{u_{i+1,j,k} - u_{i,j,k}}{\Delta x} \quad .$$

The quotients D^{-y}, D^{+y}, D^{-z} and D^{+z} are defined similarly. The denominators Δx, Δy and Δz are the voxel size along each direction.

3.2.2 Algorithm

The Fast marching algorithm provides a solution to (3.7) in $\mathcal{O}(n \log n)$ operations, where n is the number of voxels in the image. The three main characteristics of this algorithm are the following:

Causality. By fully rewriting (3.7) with the gradient approximation of (3.9), we have

$$\begin{aligned}F(x,y,z) = \quad & \max(\frac{u_{i,j,k} - u_{i-1,j,k}}{\Delta x}, \frac{u_{i,j,k} - u_{i+1,j,k}}{\Delta x}, 0)^2 \\ & + \max(\frac{u_{i,j,k} - u_{i,j-1,k}}{\Delta y}, \frac{u_{i,j,k} - u_{i,j+1,k}}{\Delta y}, 0)^2 \\ & + \max(\frac{u_{i,j,k} - u_{i,j,k-1}}{\Delta z}, \frac{u_{i,j,k} - u_{i,j,k+1}}{\Delta z}, 0)^2 \quad .\end{aligned} \tag{3.10}$$

We see from the previous expression that u_i will not depend on u_{i-1} or u_{i+1} if $u_{i-1} \geqslant u_i$ or $u_{i+1} \geqslant u_i$. In other words, the value of u at one grid point will only depend on neighbors that have a smaller u value. Using this property, the algorithm steps the solution outwards from the boundary condition.

Narrow band. Following the propagating front interpretation, the algorithm starts from the points defined by the boundary condition. In our case of shortest path problem, the boundary condition is actually expressed at the starting point. As the front propagates outwards, only the front points and their neighbors need to be accounted for at one given step. The narrow band is the set formed by these points (see Fig. 19). By solving (3.10), we find the arrival time for a front point. This updating of u only happens once for each voxel, yielding an optimally effective algorithm. This means that all points inside the contour defined by the narrow band have been updated and their u value is not to be changed. The key lies in the selection of which grid point in the narrow band to update. The causality condition tells us that it is the point with the smallest u value.

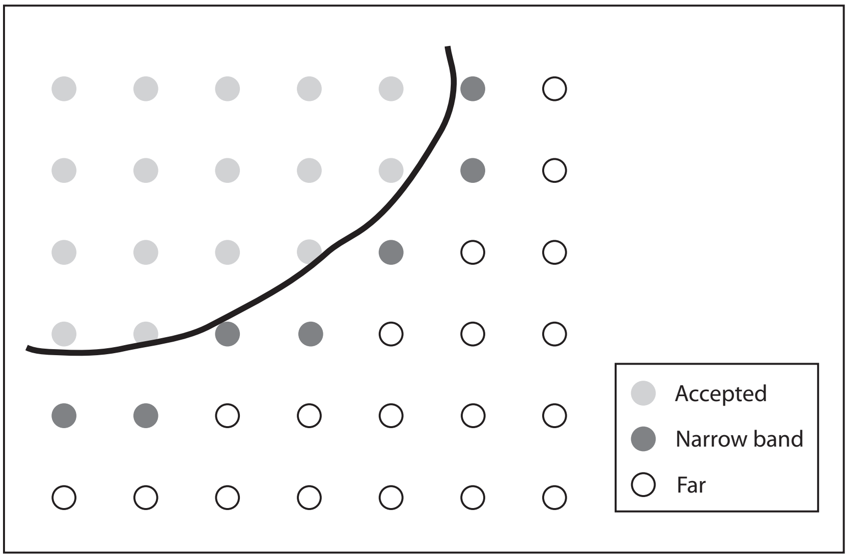

Figure 19: The front during fast marching propagation. The set of "accepted" voxels have been included in the computation and will not be visited again. The "narrow band" voxels are candidates to be included in the next iteration. The "far" voxels are ignored for the next iteration.

Priority Queue. In order to efficiently manipulate the grid points contained in the narrow band, we build a priority queue, implemented as a min-heap structure[2]. The complexity of min-heap insertions and removal is $\mathcal{O}(\log n)$, and $\mathcal{O}(1)$ for min-value extraction. The overall complexity of the fast marching algorithm is $\mathcal{O}(n \; \log n)$, making it very efficient, even on large datasets.

For more details about the implementation, see Section 4 and [34, 71, 89]. Figure 20 shows the result of a fast marching run on a 2D MIP of a 3D MRA data set from papers V and VI.

---

[2] A heap is a complete binary tree. Its top node, the root, contains the lowest value in the tree [26].

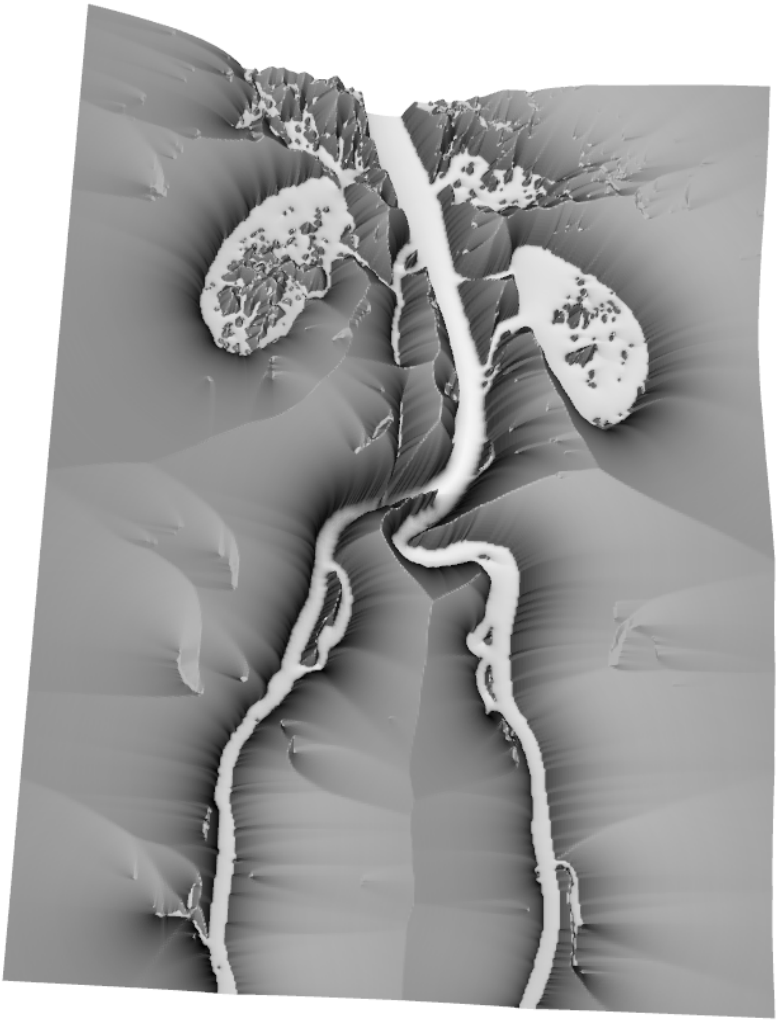

Figure 20: Example of applying fast marching to a 2D MIP image of a whole-body angiogram. The cost function is the one used in paper V. The image is a surface rendering of arrival time values, shown here as the altitude at each 2D point. The algorithm ensures that it is possible to slide back from any point in the image back to the start point, which in this case was placed at the branching of the abdominal aorta and the common iliac arteries. The rendering was produced using Paraview (Kitware Inc., Clifton Park, NY, USA).

3.2.3 Cost function

Cost function design is an essential step for the success of the fast marching procedure. The desired properties for a cost function are as follows:

- Low cost values in regions where the path should be.
- High cost values in regions where there is no reason the path should be. It should not be set to infinity though, because it can be useful for the path to be able to go through high cost areas (e.g. in case of stenosis, the path between the two disconnected branches of the stenosed vessel jumps through the flow void).
- Infinite cost values at “obstacles”, that is objects we definitely want the path to stay away from.

Examples of cost functions can be found in papers V and VI.

3.3 Vessel enhancement

In Contrast-Enhanced MR Angiography, the objects of interest are blood vessels, and in particular the arteries. They are cylindric objects, with brighter intensity than the background, due to the presence of contrast medium. One of the steps to detect arteries involves enhancement of these structures, while removing other objects, like for example kidneys. Detection and enhancement of 3D cylindrical objects has been an active research field in the last decade [6, 7, 48, 75, 77, 78, 89, 133]. The methods described in this section emerge from research in:

Differential geometry. Differential geometry is the description of shape through derivatives. Image features can be described in terms of a combination of local derivatives of the 3D grayscale image [44, 155]. In addition to that, it is desirable that these differential descriptions of shape are invariant to orthonormal transformations[3].

Scale space theory. In scale space theory, images are interpreted as observations of an infinitely smooth function (the scene), measured by a device with a given aperture [73, 92, 155, 172]. This theory elegantly solves the problem of discrete differentiation as will be seen in section 3.3.1. Extracting features by using differential operators is considered as a measurement [42]. The aperture of the measuring device is the *scale* at which the object is observed. The feature only have meaning for this particular scale. Gaussian scale-space theory gives

---

[3] As they are compositions of translations and rotations, these transformations leave angles and distances unchanged. They are represented by orthonormal matrices, for which $\mathsf{R}^{\mathsf{T}} = \mathsf{R}$ and $\|\mathsf{R}\| = 1$.

us tools to compute these features and, more important, study them over scale.

3.3.1 The Hessian matrix

A real 3D function can be approximated around a given point $\mathbf{x}_0$, using the Taylor approximation:

$$f(\mathbf{x}_0+\boldsymbol{d}) = f(\mathbf{x}_0)+\boldsymbol{d}^{\mathsf{T}}\cdot\nabla f(\mathbf{x}_0)+\frac{1}{2}\,\boldsymbol{d}^{\mathsf{T}}\cdot\mathsf{H}_f(\mathbf{x}_0)\cdot\boldsymbol{d}+\mathcal{O}(\|\boldsymbol{d}\|^3)\ , \tag{3.11}$$

where ∇ is the gradient operator, $\boldsymbol{d}$ is a small perturbation vector of $\mathbb{R}^3$, and H_f is the so-called Hessian matrix, containing the partial derivatives of f.

$$\mathsf{H}_f = \nabla(\nabla f) = \begin{bmatrix} \frac{\partial^2 f}{\partial x^2} & \frac{\partial^2 f}{\partial x\partial y} & \frac{\partial^2 f}{\partial x\partial z} \\ \frac{\partial^2 f}{\partial x\partial y} & \frac{\partial^2 f}{\partial y^2} & \frac{\partial^2 f}{\partial y\partial z} \\ \frac{\partial^2 f}{\partial x\partial z} & \frac{\partial^2 f}{\partial y\partial z} & \frac{\partial^2 f}{\partial z^2} \end{bmatrix} = \begin{bmatrix} f_{xx} & f_{xy} & f_{xz} \\ f_{xy} & f_{yy} & f_{yz} \\ f_{xz} & f_{yz} & f_{zz} \end{bmatrix}\ . \tag{3.12}$$

Equation (3.11) describes the local image structure up to the second order in terms of derivatives. The gradient determines the best linear approximation around a point, and the Hessian the best quadratic approximation. The Hessian can also be seen as the first order variation of the gradient:

$$\nabla f(\mathbf{x}_0+\boldsymbol{d}) \simeq \nabla f(\mathbf{x}_0)+\mathsf{H}_f(\mathbf{x}_0)\cdot\boldsymbol{d}\ . \tag{3.13}$$

The Hessian tells us how the gradient vector changes as a function of displacements away from the point at which it is measured. Those displacements and the resulting gradient changes are both vectors in 3D. More on the local structure can be found for example in [53]. One interesting property is that the Hessian can be used to calculate the second derivative of f along any direction:

$$f_{vv} = \boldsymbol{v}^{\mathsf{T}}\cdot\mathsf{H}_f\cdot\boldsymbol{v}\ , \tag{3.14}$$

To further study the structure of the Hessian matrix, its eigenvalues and its associated eigenvectors are computed. This can be done at each point, and it is equivalent to a 3D rotation of the coordinate system at that point, so that the Hessian expressed in the local coordinates is diagonal. As H_f is symmetric and real, the diagonalization is always possible. This new coordinate system is called the second order gauge coordinates. We then have an orthogonal matrix R such that

$$\mathsf{R}^{\mathsf{T}} \cdot \mathsf{H}_f \cdot \mathsf{R} = \begin{bmatrix} \lambda_1 & 0 & 0 \\ 0 & \lambda_2 & 0 \\ 0 & 0 & \lambda_3 \end{bmatrix} \quad . \tag{3.15}$$

We will use the convention $|\lambda_1| \leqslant |\lambda_2| \leqslant |\lambda_3|$ in the following. The eigenvalues of H are invariant to orthonormal transformations, and thus constitute a good set of descriptors for the second order local structure of an image.

Extracting the derivatives of a scene f from the image is an ill-posed problem [42]. This means that an arbitrarily small local perturbation of a function f at a point of its domain can cause an arbitrarily high error in the computation of the partial derivatives of f at that point. But differentiation can be achieved in a well-posed manner by convoluting the image with Gaussian derivative kernels G_σ [155]. This way, the derivatives are only relevant when computed at a given scale σ. For example:

$$\frac{\partial f}{\partial x} \simeq G_{x,\sigma} * f = \frac{\partial G_\sigma}{\partial x} * f \quad , \tag{3.16}$$

where

$$G_\sigma(\mathbf{x}) = \frac{1}{(2\pi\sigma^2)^{D/2}} e^{-\|\mathbf{x}\|^2/2\sigma^2} \quad , \tag{3.17}$$

and D is the dimensionality of the image, usually $D = 3$ in our case. The Taylor approximation then becomes:

$$f(\mathbf{x}_0 + \boldsymbol{d}; \sigma) = f(\mathbf{x}_0) + \boldsymbol{d}^{\mathsf{T}} \cdot \nabla f(\mathbf{x}_0; \sigma) + \frac{1}{2}\, \boldsymbol{d}^{\mathsf{T}} \cdot \mathsf{H}_f(\mathbf{x}_0; \sigma) \cdot \boldsymbol{d} + \mathcal{O}(\|\boldsymbol{d}\|^3) \quad . \tag{3.18}$$

3.3.2 Ridges

The common language definition of a ridge is “a top or upper part, especially when long and narrow”. Ridges are an intuitively simple concept but their mathematical definition is not well agreed upon. There has been many attempts to give this concept a mathematical definition that can be used in image analysis. A full review of this topic is outside the scope of this thesis, and we will refer the reader to the works by Eberly [37, 37], Lindeberg [93], Koenderink [74] and Lopez [95, 96] for different approaches to the notion of ridge. We focus on methods using classification techniques applied to the Hessian eigenvalues and realize that, in 3D, a ridge is characterized by:

$$\begin{cases} \lambda_1 \simeq 0 \\ |\lambda_1| \ll |\lambda_2| \quad \text{and} \quad |\lambda_1| \ll |\lambda_3| \\ \lambda_2 \simeq \lambda_3 \end{cases} \quad . \tag{3.19}$$

That is:

- The smallest eigenvalue is almost zero: there exists a direction, determined by the corresponding eigenvector, along which the second derivative is close to zero.
- The derivatives are significantly non-zero in the plane perpendicular to this direction.
- They are moreover similar, which means the local structure of the image shows a high degree of symmetry in this plane. This is desirable to detect vessels, as results have indicated that most of the luminal cross-section of stenosed coronary vessels are circular or elliptical [17].

Krissian [78] showed with an analytic model of a vessel that, using the λ_i, we could build a filter whose response is maximal at the center of the vessel, and smoothly decreases towards the boundary. We will next describe one such filter, that was used to identify vessels in paper VI.

3.3.3 The vesselness filter

The idea of using the eigenvalues of the Hessian matrix to detect locally cylindrical structures in 3D was first reported in [58, 75, 98, 133]. From this work, Frangi [45, 48] developed a “vesselness filter”, which is a measure of how close to a bright cylinder the neighborhood around a given point is. It has become a well-accepted descriptor for vessel objects [35, 57, 161, 174]. It is defined as

$$\mathcal{V}(\mathbf{x};\sigma) = \begin{cases} 0 \quad \text{if} \quad \lambda_2 < 0 \quad \text{or} \quad \lambda_3 < 0 \\ (1 - e^{-\mathcal{R}_A^2/2\alpha^2}) e^{-\mathcal{R}_B^2/2\beta^2} (1 - e^{-\mathcal{S}^2/2c^2}) \quad \text{otherwise}, \end{cases} \tag{3.20}$$

where

$$\mathcal{R}_A = \frac{|\lambda_2|}{|\lambda_3|} \qquad \text{cross-sectional asymmetry,}$$

$$\mathcal{R}_B = \frac{|\lambda_1|}{\sqrt{|\lambda_2 \lambda_3|}} \qquad \text{blobness,}$$

$$\mathcal{S} = \sqrt{\sum_j \lambda_j^2} \qquad \text{degree of image structure (Fröbenius norm),}$$

and λ_1, λ_2, and λ_3 are the three eigenvalues of the Hessian matrix, ordered so that $|\lambda_1| \leqslant |\lambda_2| \leqslant |\lambda_3|$. One can easily see that (3.20) actually gives high values for eigenvalue triples corresponding to the ridge criteria given in (3.19). Figure 21 shows an example of vesselness computation. As the vesselness value is computed at a given scale, it corresponds to the action of “probing” the volume with a “cylinder detector” for a given cylinder diameter.

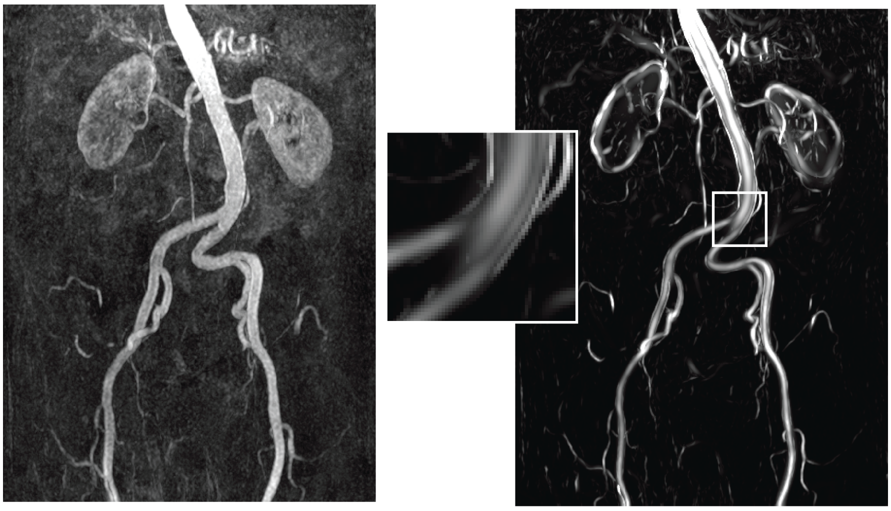

Figure 21: Vesselness results from a 3D MRA data set. The left image is a MIP of the original volume. The right image is a MIP of the vesselness volume, first along the scale direction, and then along the front-to-back direction. A branching region is magnified to show that, being a discriminant function based on second degree differential operators, it does not emphasize bifurcations, which are third degree structures.

For the filter to be really useful, it has to be computed across a range of different scales, corresponding to the objects present in the image. Two parameters have to be chosen with care:

- The upper and lower bounds of σ. Their selection is important because not every scale is relevant. The upper bound $\sigma_{\max}$ determines the region of capture of the vessel detector and is set equal to the maximum vessel radius we want to detect. The lower bound $\sigma_{\min}$ is set to one, so that it corresponds to structures of size comparable to the voxel size.
- The step size while sampling along the scale direction. A straightforward linear sampling is not appropriate because this might lead to aliasing at fine scales and over-sampling at coarse levels of scale. The scale dimension should be sampled exponentially [44, 91]. We usually choose powers of 2: $\sigma \in \{\sigma_{\min} = 1, 2, 4, 8, 16, 32 = \sigma_{\max}\}$.

This study of the whole set of vesselness responses forms a 4D data set, that we used in paper VI to detect vessel centerlines, following the approach described in [171]. In order to be able to compare the vesselness values across scales, we need to use normalized derivatives [92, 94]. That is:

$$\frac{\partial f}{\partial x} = \sigma\, G_{x,\sigma} * f \tag{3.21}$$

and

$$\frac{\partial^2 f}{\partial x^2} = \sigma^2\, G_{xx,\sigma} * f \ \ . \tag{3.22}$$

This is to compensate for the averaging effect of Gaussian convolution with large scale kernels. We used the notation $G_{xx,\sigma}$ for the second derivative relative to x of the Gaussian kernel of (3.17).

3.4 Measurement of vessels

We mentioned in section 2.1 that a quantitative knowledge of vascular morphology is important for the diagnosis, treatment and follow-up of atherosclerosis. So far, the focus has been on measuring the degree of stenosis, that is the degree to which luminal diameter is reduced. It is an important clinical measurement used to evaluate the opportunity of surgical treatment. Similarly, in some cases of vascular aneurysms[4], the largest cross-sectional area determines the potential need for surgical intervention.

In clinical practice, stenoses are still measured either directly on film with a caliper, or on a computer screen, using more or less advanced “measuring tools”. Although measurements of stenosis based on visual estimates or caliper determinations from angiograms are useful, they are not precise, as noted already in 1976 by Zir [176]. Manual measurements also suffer from poor reproducibility. Two large scale clinical trials have suggested a standardized measure of stenosis: the North American Symptomatic Carotid Endarterectomy Trial (NASCET [1]) and the European Carotid Surgery Trial (ECST [2]). They are schematically represented in Fig. 22.

Efforts have also been done towards the automatic quantification of stenosis, using image analysis [22, 47, 59, 68, 160, 169, 173]. However, it has been shown that plaque vulnerability, that is its tendency to rupture and thereby cause a potentially acute event, is not well predicted by a lowered vessel area [116]. The reasons are:

- Outward remodeling: the vessel wall responds to flow variations by increasing its outer diameter.
- Plaque constitution and geometry may be more important than lumen size [124, 151].

---

[4] An aneurysm is a bulge (dilation) in the wall of an artery. The bulge usually occurs in a weak area of the artery’s wall. The pressure of blood inside the artery forces the weak area to balloon outward.

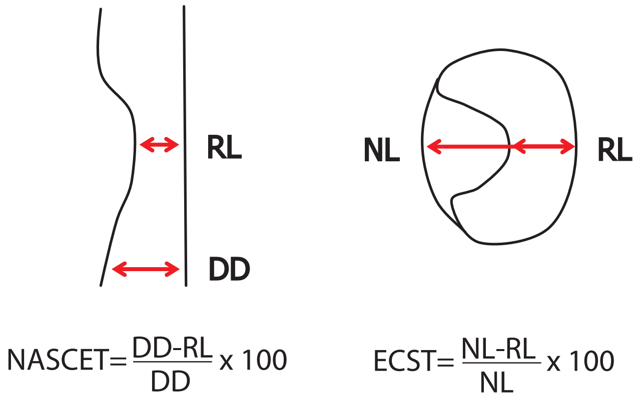

Figure 22: The two stenosis measurement methods that have been shown by large-scale clinical trials to be relevant: left, the NASCET measure, where RL is the residual lumen diameter and DD is the diameter distant to the stenosis; right, the ECST measure, where NL is the normal lumen diameter estimated at the stenosis location.

This means that more global measures of vessel morphology can be of interest. Description of such measures and ways to practically implement them are the purpose of paper VI. We propose indexes measuring the geometry of the vessel centerline, modeled as a 3D curve.

3.4.1 Measures along the central axis

The methods described in section 3.2 and 3.3 have given us a line representation of the main branches of the arterial tree. It is a graph consisting of vessel centerlines of the main arteries, and a set of nodes at the junction of the centerlines. A 3D curve (see Fig. 23) $\mathcal{C}$ in $\mathbb{R}^3$ is fully characterized by its curvature and torsion. Given a parametrization of $\mathcal{C}$, where each point of $\mathcal{C}$ is identified by its coordinate vector $\boldsymbol{r}(t)$, the curvature $\kappa(t)$ and the torsion $\tau(t)$ are defined as

$$\kappa(t) = \frac{\|\dot{\boldsymbol{r}} \times \ddot{\boldsymbol{r}}\|}{\|\dot{\boldsymbol{r}}\|^3} \quad \text{and} \quad \tau(t) = \frac{\dot{\boldsymbol{r}} \cdot (\ddot{\boldsymbol{r}} \times \dddot{\boldsymbol{r}})}{\|\dot{\boldsymbol{r}} \times \ddot{\boldsymbol{r}}\|} \,, \tag{3.23}$$

where $\dot{\boldsymbol{r}}, \ddot{\boldsymbol{r}}, \dddot{\boldsymbol{r}}$ represent the derivatives of $\boldsymbol{r}$ with respect to the parameter t. κ and τ can be geometrically interpreted as follows:

curvature. Curvature is the amount by which a curve deviates from being a straight line. The circle which shares the same tangent as the curve at a given point is called the osculating circle. The curvature is then

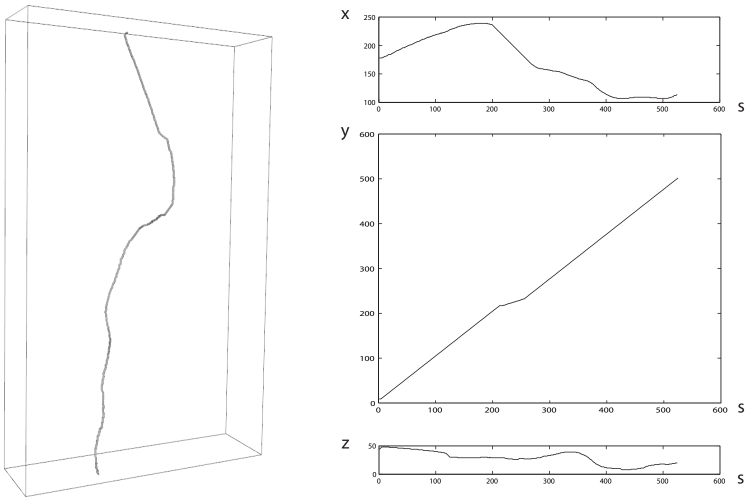

Figure 23: The 3D path. It is represented as a 3D curve on the left, and, on the right, as the x, y, and z values of $\boldsymbol{r}$ plotted against the arc length parameter.

$\kappa = 1/R$, where R is the radius of the osculating circle. The larger the curvature, the smaller the osculating circle, and therefore the faster the curve is turning. A circle of radius R obviously has constant curvature $1/R$, while a straight line has curvature zero.

torsion. The torsion of a curve measures how sharply it is twisting. Torsion is related to the amount of helicoidal deformity in the centerline (and especially to the pitch of that helix). It measures the amount of deviation of the curve from a single plane, and is thus a measure of planarity. The torsion is zero for a circle, zero for a straight line, and is maximum for a circular helix whose pitch is the same as the radius of its basic circle. Another interpretation is that τ measures the rate at which the osculating plane changes direction.

The derivatives of $\boldsymbol{r}$ are computed using 1D Gaussian derivative kernels, similarly to the differentiation method used in 3D to compute the Hessian.

The variance of the derivative kernel determines the degree of regularization. We chose a variance of 3 for our computations. Spatial anisotropy is handled by using a higher variance along the z-direction. Coeurjolly recently suggested a discrete method to compute curvature [24], but there does not exist, as far as we know, an equivalent algorithm to compute torsion.

4 Implementation

The difficulty of mathematical image processing lies in applying methods that have originally been derived for continuous spaces (e.g. differential geometry) to images, that are discrete in essence. The purpose of this section is to describe how the actual work is done, taking into account the discrete nature of the data we work with.

All methods described in this thesis have been implemented as plugins to ImageJ [125]. ImageJ is a public domain package written in Java, originally designed for biological image analysis, mainly microscopy. In this section, we will give a more practical description of the developed algorithms, and also describe how we implemented the interaction between users and angiographic data. The following plugins, among others, have been developed and are freely available from the author:

- Grayscale connectedness and its seeding interface
- Fast marching on anisotropic grids in 2D to 4D
- An interface to place seed points in a MIP
- Vesselness filter

We chose ImageJ because it is a lightweight but very powerful image application. It is highly portable, as it is written in Java, and can thus be used on many combinations of hardware and operating systems. In addition, its speed of execution makes ImageJ very competitive in comparison with C++ based image analysis libraries. Last but not least, the fact that ImageJ is a public domain program gives us, at no cost, access to a whole set of imaging functions and to a programming community willing to exchange their knowledge.

4.1 Grayscale connectedness

The computation of grayscale connectedness, as described in section 3.1, requires the user to provide a set of seed points. These seeds are the starting point of a region growing-like procedure. They represent anatomical knowledge from the expert, and are crucial for the success of grayscale connectedness segmentation.

4.1.1 User interface

In paper V, we introduced a method to place seed points in a 3D volume by using, in parallel, a MIP and the original volume. Using the interface shown in Fig. 24, the operator can place seed points in the MIP or in the original volume. Seed points will show up in both windows, as the relocation from 2D to 3D (MIP to MPR) is performed automatically.

Depending on the complexity of the data set and the number of different objects one wants to individualize, interaction times range from 5 to 15 minutes for a whole 3D volume.

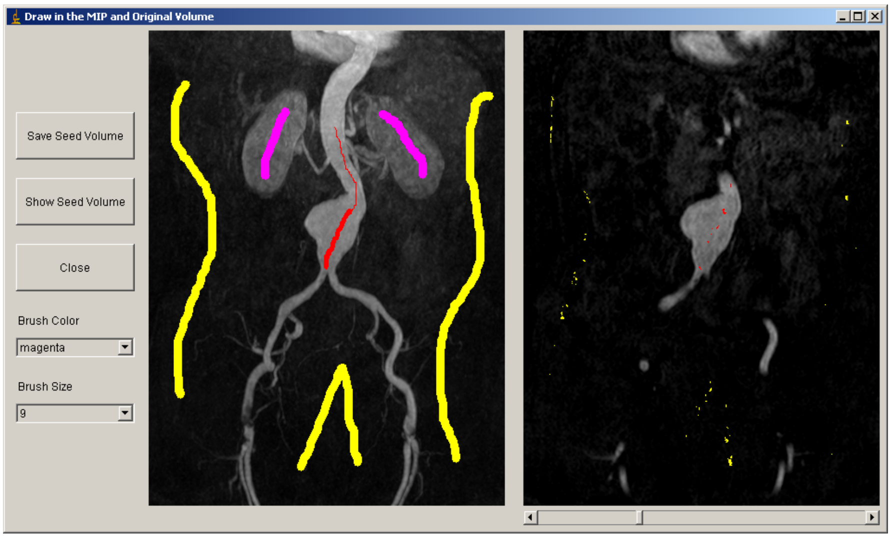

Brush Color
magenta

Brush Size
9

Figure 24: Interface to place seed points in the MIP, as described in paper II. The left window shows the MIP with the different seed regions, and the right window shows the original volume as a MPR. The user is able to paint in both windows, as the program relocates seed voxels between windows.

4.1.2 Algorithm

The algorithm is described p. 49. As grayscale connectedness is an iterative process, it is not possible to give a reliable estimate of the computational complexity of this algorithm. However, the experience showed that 10 to 50 iterations were usually enough to achieve good segmentation results. This corresponds to computation times ranging from 2 to 15 minutes on a commercial PC.

4.2 Fast marching

Fast marching is an algorithm we used in papers V and VI to find a curve within the artery joining two given points. It solves the “one source, multiple destinations” shortest path problem, given a positive cost function (see section 3.2). The algorithm we implemented is detailed by algorithms 2 and 3. It actually is a more general version of fast marching than what is usually described, as we do not assume isotropic sampling of the cost function. It makes the updating procedure of algorithm 3 slightly more complicated, but

Algorithm 1: The grayscale connectedness algorithm in 3D

```
Input: input image, $I$ with grayscale function $f_I$
label image $color_I$ (with $n$ seeded regions $S_j$)
output image, $O$ with grayscale function $f_O$
label image $color_O$ (both initialized to 0)

foreach $v \in S_j, 0 < j \leq n$ do
    $f_O(v) = f_I(v)$
    $color_O(v) = color_I(v)$
repeat
    for $v = (1,1,1)$ to $(x_{\max}, y_{\max}, z_{\max})$ , $v \notin S_j$ do
        Find $w_{\max} \in \mathcal{N}^+(v)$ such that $f_O(w_{\max}) = \max_{w \in \mathcal{N}^+(v)} (f_O(w))$
        if $f_O(w_{\max}) > f_O(v)$ then
            $f_O(v) = \min\{f_I(v); f_O(w_{\max})\}$
            $color_O(v) = color_O(w_{\max})$
    for $v = (x_{\max}, y_{\max}, z_{\max})$ to $(1,1,1)$ , $v \notin S_j$ do
        Find $w_{\max} \in \mathcal{N}^-(v)$ such that $f_O(w_{\max}) = \max_{w \in \mathcal{N}^-(v)} (f_O(w))$
        if $f_O(w_{\max}) > f_O(v)$ then
            $f_O(v) = \min\{f_I(v); f_O(w_{\max})\}$
            $color_O(v_O) = color_O(w_{\max})$
until nb of changes in O $\leq MinNbChanges$
```

more adapted to the problems we want to solve. The necessity of implementing this particular version of fast marching has two reasons:

- Our datasets are large. The volumes we work with are $384 \times 512 \times 60$ in size, with a voxel size of $0.8 \times 0.8 \times 2$. A proper use of the usual implementation of fast marching would require a resampling of our volume to $384 \times 512 \times 150$. If a 32-bits version of a given volume is to be kept in memory, it would represent 112 MB instead of the non-resampled 45 MB.
- We work in four dimensions. We use fast marching in 4D = 3D + scale-space in paper VI. The hypervolumes are $384 \times 512 \times 60 \times 7 \times$ 32b, which represents 315 MB of input data only. Adding the size of the output image and the algorithm's data structures, it clearly becomes difficult to handle for a commercial PC.

We used the freely available library JDSL to implement the min-heap data structure of the narrow band.

The updating procedure of the fast marching algorithm consists in solving (3.10), that is, finding the largest possible solution to the following quadratic equation:

$$\left(\frac{u_{i,j,k} - u_x}{\Delta x}\right)^2 + \left(\frac{u_{i,j,k} - u_y}{\Delta y}\right)^2 + \left(\frac{u_{i,j,k} - u_z}{\Delta z}\right)^2 = F^2 \quad , \tag{4.1}$$

where

$$\begin{cases} u_x & = & \min(u_{i-1,j,k}, u_{i+1,j,k}) \\ u_y & = & \min(u_{i,j-1,k}, u_{i,j+1,k}) \\ u_z & = & \min(u_{i,j,k-1}, u_{i,j,k+1}) \quad . \end{cases} \tag{4.2}$$

Fast marching is used to compute the "arrival time map", given a cost function and a pair of start and end points. Its computation time depends highly on the discriminant power shown by the cost function. Using a cost function based on vesselness values, fast marching finds within a few seconds the shortest path between two vessel points across a $384 \times 512 \times 60$ image.

4.3 Vesselness

The results from the vesselness filter were used in paper VI to build the cost function used as input to fast marching. As described in section 3.3, computing vesselness requires the computation of second-order derivatives, using the Gaussian scale-space framework, and the computation of eigenvalues of a 3×3 matrix at each voxel. We used E. Meijering's plugins to ImageJ [105] to implement all derivative computations, and the JAMA matrix package

Algorithm 2: Pseudo-code describing the Fast Marching main loop.

```
input  : a list of seed points, and a cost image F
output: an image u of arrival time values

// Initialization
foreach $v \in F$ do
    if $v \in list$ then
        u (v) = 0
        label (v) = TRIAL
    else
        u (v) = $\infty$
        label (v) = FAR
// Main loop
while narrowBand is empty do
    voxel = getMin (narrowBand)
    neighbors = listNeighbors(voxel)
    foreach nVoxel $\in$ neighbors do
        newU = computeNewU (nVoxel)
        if label (nVoxel) = FAR then
            changeLabel(nVoxel, TRIAL)
            u ( neVoxel ) = min ( u ( nVoxel ), newU )
            insert (narrowBand, newU, nVoxel)
        if label (nVoxel) = TRIAL then
            u ( nVoxel ) = min ( u ( nVoxel ), newU )
            replace (narrowBand, newU, nVoxel)
    remove (narrowBand, voxel)
```

Algorithm 3: Pseudo-code describing the Fast Marching updating procedure ComputeNewU. It is inspired from [34]. The algorithm is valid for volumes with non-isotropic spatial resolutions. Note that the implementation is more verbose, as the elegant simplifications suggested in [71] or [104] cannot be applied.

```
// Initialization
Compute $u_x$,$u_y$, and $u_z$ (see (4.2))
Sort and put them into an array a such that $u_3 \geqslant u_2 \geqslant u_1$
Sort the $\Delta x, \Delta y, \Delta z$ accordingly into $\Delta_{1,2,3}$

Delta (EQ3): discriminant of
$\left(\frac{u-u_1}{\Delta_1}\right)^2 + \left(\frac{u-u_2}{\Delta_2}\right)^2 + \left(\frac{u-u_3}{\Delta_3}\right)^2 = F^2 \quad (EQ3)$
if Delta (EQ3) $\geqslant 0$ then
    possible_u = largestRoot(EQ3)
    if possible_u $\geqslant u_3$ then
        // u depends on 3 neighbor directions
        return possible_u
    else
        GOTO Case2
else
    Case2
    Delta (EQ2): discriminant of
    $\left(\frac{u-u_1}{\Delta_1}\right)^2 + \left(\frac{u-u_2}{\Delta_2}\right)^2 = F^2 \quad (EQ2)$
    if Delta (EQ2) $\geqslant 0$ then
        possible_u = largestRoot(EQ2)
        if possible_u $\geqslant u_2$ then
            // u depends on 2 neighbor dir.
            return possible_u
        else
            Case1
            // u depends on 1 neighbor dir.
            return $u_1 + \Delta_1 F$
    else
        GOTO Case1
```

for eigenvalues computation. The detailed description of discrete Gaussian scale-space implementation is not given here, but it should be noted that a correct solution to the problem is not straightforward (see for example Lindeberg's book on the subject [92]).

For a $384 \times 512 \times 60$ volume, and using anisotropic Gaussian kernel sizes to reflect the spatial anisotropy of the input volume, computation of the vesselness filters takes around 3 min per scale on a PC with a 3 GHz processor and 2 GB of RAM. That means that in our experiments, where the vesselness was computed at 6 scales, the computation time for one whole-body data set was about 80 minutes.

5 Conclusions and future research

With the exception of an incursion in the realms of CT imaging in paper II, this thesis aims at providing tools to make better use of information in MRA images. Two projects, centered on two imaging protocols, constitute this thesis. We will discuss them separately.

5.1 Arteries-veins separation in BP-CE-MRA

We have proposed a method that helps radiologists visualize complex 3D structures like vessel trees, by separating arteries and veins in BP-CE-MRA. It uses user interaction, grayscale connectedness and maximum intensity projections. The algorithms are simple to implement, have low memory requirements, and converge quickly towards the solution. Moreover, concurrent grayscale connectedness provides a complete segmentation of the volume in only one pass. Yet, it does not completely solve the problem of "leakage" between arteries and veins at locations where contrast is poor between vessels. This is actually a limitation in the resolution of the imaging procedure, and can only efficiently be solved by model-based techniques [8, 46, 161]. Another limitation is the rather long interaction time required, still above the threshold that would make the method clinically useful. This can be addressed by automatically detecting features (e.g. vesselness) to identify the seed points, and with better interaction capabilities, as shown in paper III. The rather simplistic definition of connectedness is also a drawback, but it can be generalized [31, 32, 132, 158] to be applicable to other segmentation tasks [117, 164]. To date, the most successful application of computerized image analysis to solve the same kind of problems use a combination of feature detection, vessel models and level set techniques [161]. As the Blood-Pool agents are getting closer to entering the market, those techniques still need to improve to reach clinical acceptance.

5.2 Whole-body CE-MRA

The systemic nature of atherosclerosis calls for an imaging technique that offers full body coverage within an acceptable time. The downside is that the amount of data becomes difficult to handle, as does the task of understanding its 3D structure. We showed that user interaction, in cooperation with image analysis, could provide a hint of an answer to the question: "is this patient at risk of an atherosclerosis-related event?". A more argued answer to this question needs further clinical investigations.

The whole-body MRA protocol is relatively recent, and there is room left for improvement [20, 85]. Concerning vessel detection, there are still theoretical questions that need to be answered, like the detection and proper handling of vessel branches. This work is closely related to research on medialness computation [107, 118] and grayscale skeletons [27, 175].

5.3 Future work

Much work has been done since the first reports on automated vessel analysis [12, 109, 114, 131, 149]. However, a significant amount of research is still needed for these methods to be clinically useful. Advances are needed on the medical imaging front (MI), and on the image analysis front (IA):

MI MR imaging offers the extended possibility to study the inner structure of tissues. There is a tendency towards exploring the composition and local structure of atherosclerotic plaque to measure its vulnerability [39, 124]. Functional plaque imaging allows to relate local mechanisms to more global measures like the ones we suggest, for a better understanding of atherosclerosis pathophysiology.

IA Some recent work on resolution of Hamilton-Jacobi equations showed that sweeping algorithms may outperform queue-based algorithms [156, 168]. This means that the way we use grayscale connectedness would be an efficient algorithm to handle more general definitions of connectedness, like the fuzzy connectedness framework described by Udupa [112, 132, 158]. Fuzzy Connectedness is a powerful, all-purpose segmentation algorithm, that makes few assumptions about the data. It may benefit from an attractive property of the chamfer algorithm: its low memory requirements. Despite the growing availability of computing power, memory is always a concern when manipulating large medical datasets.

IA The vesselness filter introduced by Frangi identifies cylinder-like local neighborhoods with a discriminant function of the Hessian's eigenvalues. It is possible to generalize this approach, as suggested recently by Lillholm [88], by feeding the whole set of derivatives up to a given order to a classification algorithm. There is however a great deal of work to be done on the choice of the classifier, the possible normalization between the different features, or the way scale should be handled.

IA From our work on centerline detection in whole-body angiograms, we feel that the next step in analyzing the 3D structure of the vascular tree is segmentation. This way, more descriptors of the vessel wall geometry could be gathered and compared to other, more conventional, clinical tests (e.g. biochemical markers). The geometric approach could also be compared with more local analysis of stenoses (see section 3.4 for references).

The task is far from trivial: the main obstacles are resolution and grayscale normalization of MR images. Whole-body MR images are still

> quite poorly resolved, and not adequate to measure small objects like peripheral arteries [60, 135]. In addition, in MR imaging, voxel intensities of similar tissues are not comparable between scanners, not even between patients imaged by the same scanner, and not even within a single image. This is due to hardware-induced and patient-induced variations in the measured signal. It is even more apparent in angiography, where voxel intensities are proportional to the concentration of contrast medium. This makes the use of simple segmentation methods like thresholding impossible. That is why successful attempts to segment MR images rely on a careful combination of low-level operators and model-based techniques [61].
>
> With a proper segmentation of whole-body angiograms, it would be possible to measure for example local defects in concavity [111] or surface roughness [146, 147] to obtain an estimate of the global plaque burden [150].

It seems that our research has led to more questions than answers. But some may argue that this is the purpose of research.

5.4 Conclusion

The use of automated image analysis methods as a clinical tool, that is, used everyday by a physician with little knowledge of image analysis, is only at its early dawn. There is a didactic work that needs to be done, to explain the advantages and limitations of computerized image analysis. It is also important to work on the interface: it should be easy to interact with and should display the needed information. That way, our work will help improve the quality of diagnostic. Better analysis and better visualization, for a better understanding.

6 Summary of the included papers

This section presents the content of each of the enclosed papers, giving an more detailed presentation than the abstract. It also includes the main results, giving an overview of the achieved work.

6.1 Papers I and II: Grayscale Connectedness Segmentation in MRA and CTA

In the first two papers, we studied the feasibility of using the grayscale connectedness algorithm to enhance visualization of two recently introduced imaging techniques:

- Blood-pool agent CE-MRA. The new contrast agents stay in the blood stream for a longer period of time, compared to the Gadolinium compounds. This allows longer acquisition times, and consequently better resolution, also leads to better venal enhancement. For a better understanding of these images, arteries and veins can be visualized separately from each other.
- Coronary CTA. High resolution is the first requirement to produce useful images of the coronary arteries. CTA offers this possibility, together with a procedure that is potentially less hazardous for the patient than conventional angiography. Segmentation allows to use Maximum Intensity Projections to visualize these datasets, producing images similar to invasive angiography. Moreover, a separate rendition of the different branches of the coronary arteries would help a radiologist to better study them.

The complex datasets (see Fig. 25 for MRA and Fig. 26 for CTA) are very difficult to interpret with conventional rendering methods, and a segmentation step preliminary to visualization may help understand the 3D structure of the data.

The proposed algorithm uses the grayscale degree of connectedness as a tool to find the zone surrounding each vessel, in order to split the original volume into its different vessel components. In contrast to traditional segmentation methods, no grayscale information is lost in the process. Seed points of different colors are placed in the different objects of interest that need to be separated from each other. The interface allows placing these seed points either in the original volume, or in the MIP, or in both simultaneously. The algorithm then uses the defined seed points to partition the initial volume into a chosen number of Regions of Interest (ROI). Finally, visualization is achieved by MIP, Surface Rendering, or Volume Rendering. Some examples of the achieved results are presented in Fig. 25 for BP-CE-MRA and Fig. 26 for coronary CTA. In both cases, the segmentation step improves

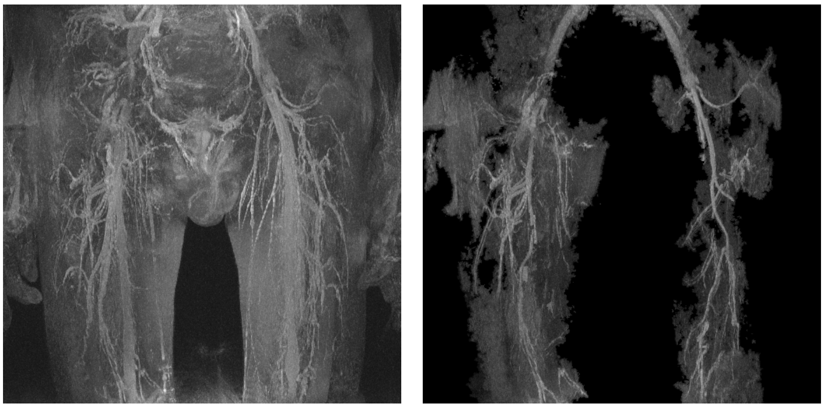

(a) (b)

Figure 25: A MRA dataset using blood pool agent as contrast medium. (a) MIP of the original volume, showing the arteries, veins, bladder and soft tissues. (b) MIP of the segmented arteries and some remaining soft tissues.

the visibility of the clinically relevant structures by subdividing them or removing unwanted objects. The interaction times necessary to produce results of high quality are around 30 min for each data set. Computation times for the GC segmentation lie around 5 to 10 min. These feasibility studies show that complex datasets can be visualized efficiently by adding an additional segmentation step. The time needed to perform this segmentation is not yet clinically tractable. However, the use of more advanced user interaction techniques (see paper III) and feature detection (as the vesselness filter used in paper VI) could make this a useful clinical tool.

6.2 Paper III: Haptic-Guided Seeding of MRA Images for Semi-Automatic Segmentation

It is difficult to efficiently visualize and interact with 3D data. In this paper, we investigate how stereo graphics and haptics can be combined to facilitate the seeding procedure in semi-automatic segmentation of magnetic resonance angiography (MRA) images. Real-time volume rendering using maximum intensity projections (MIPs) was implemented together with a haptic rendering method that provides force feedback based on local gradients and intensity values (see Fig. 27). This combination allows a user to trace vessels in the image, guided by haptic feedback. As the amount of resistance from the device is proportional to image gradient, it is easy to follow a vessel all the way across the image. This way, a user can place seed points directly in the 3D data set. We then tested two segmentation algorithms that use the set

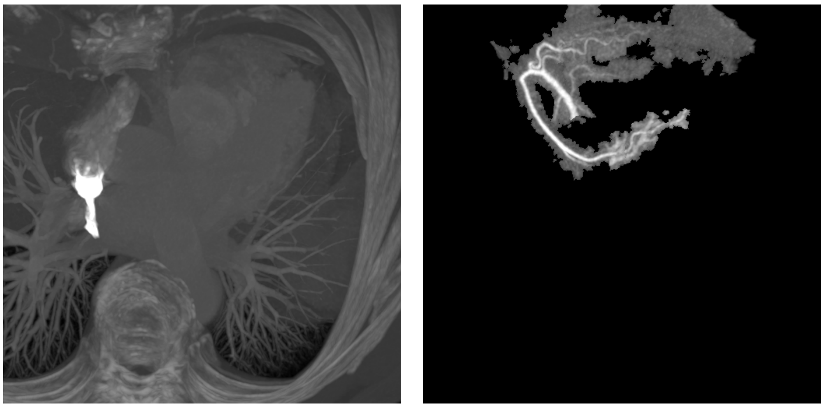
(a) (b)

Figure 26: A coronary CTA dataset. (a) MIP of the original volume, where the coronary arteries are completely masked by other, brighter components in the image. (b) MIP of the segmented right coronary artery.

of seed points as input. The seeding work burden was significantly reduced with the haptics platform. The interface provides an intuitive access to 3D data and showed the benefits of haptic interaction over conventional input devices.

6.3 Paper IV: Compensation for Geometrical Hardware-Induced Distortion in Contrast Enhanced Whole-Body Magnetic Resonance Angiography

In contrast-enhanced whole-body Magnetic Resonance Angiography (MRA), a patient's main arterial system can be imaged using an optimized MR sequence. This sequence scans the whole volume in about 87 seconds using only four stations with large FOVs (450 mm) and small image overlaps. Usage of large FOV introduces significant hardware-induced geometrical distortion to the acquired volume. The purpose of this study was to model this geometrical distortion and to create a non-linear transformation which compensates for it in post-processing.

A special MRA sequence was used on a 1.5 T Philips Gyroscan NT to acquire the volumes. A two-dimensional phantom was constructed and used to image the distortion from this MRA sequence. Distortion symmetry was assumed in head-feet direction and rotational symmetry was assumed around the scanners main axis. The phantom was scanned with different orientations to give all distortion information needed. The geometrical distortion was compensated for in the four stations and the results were added creating a distortion compensated whole-body volume. The compensation was tested

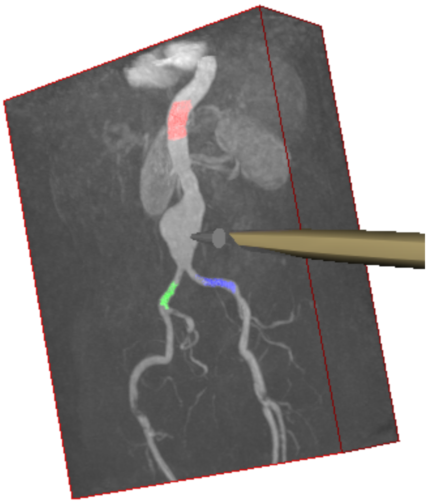

Figure 27: Volume rendering with 3D texture mapping. Here, a MIP of the abdominal vascular system is shown together with the graphical representation of the PHANTOM stylus.

on both phantom and patient volumes and the results were evaluated both visually and by extracting statistical information. Geometrical correctness of phantom volumes were measured by approximating straight lines to phantom rods. In patient volumes, the direction change of arteries was manually measured on station borders. The image continuity was evaluated visually in regions close to station borders.

Visual evaluation confirmed an improvement to the geometry of the resulting volumes. The maximum displacement of data was reduced from 16.1 mm to 2.1 mm when the compensation is performed on a phantom volume. The mean direction change of arteries over station borders was reduced from 21.0° to 2.4°. The continuity of the imaged organs was evaluated visually in regions close to station overlaps and was found to have increased.

We have shown that it is possible to compensate for the hardware-induced geometric distortion in a specific MRA sequence using a two-dimensional phantom and symmetry assumptions. The accuracy of the symmetry assumptions is of great importance and was found sufficient for present needs. However, the assumed rotational symmetry is not ideal, thus using a three-dimensional phantom with higher precision is recommended for a more accurate result. Compensation for intensity distortions can also be made with this technique using a phantom. Patient-induced distortions were not compensated for.

6.4 Paper V: Identification of the Main Arterial Branches in Whole-Body Contrast-Enhanced MRA in Elderly Subjects Using Limited User Interaction and Fast Marching

As atherosclerosis is a global disease, it becomes interesting to provide clinicians with imaging techniques that offer full coverage of the patient's arterial system.

In this paper, we suggest a method to extract, from a whole-body CE-MRA data set, a predefined set of "arteries of interest". Maximum Intensity Projections are used as an interface with the 3D volume, to place a series of landmarks inside the main arteries. The number of landmarks is kept low (36 for a whole-body data set) to reduce interaction time. The location of these landmarks is determined in advance, in cooperation with angiographers, to include the arteries with high diagnostic potential. The landmarks also represent topologically significant points in the arterial structure. The original image is automatically thresholded, providing a rough estimate of the vascular region. A distance transform of the "vascular object" is computed to build a volume where high grayscale values will be observed near the center of the lumen, low grayscale values at the vessel wall, and zero outside vessels. By taking the inverse of this image, we have a reasonable cost function for a fast marching algorithm, where it will be fastest to march through vessel voxels near the lumen center, and almost forbidden to march outside the vessel.

We tested our method on 10 subjects. It was able to build a graph model of the main arterial branches, and performed well in the presence of vascular pathologies, such as stenoses and aneurysms. Results were rated by an experienced radiologist, with an overall success rate of 82%. These rates ranged from 40% to 100%, showing that some regions, e.g. the vertebral arteries, were typically more problematic than others.

To conclude, we showed it was possible to extract chosen arterial branches in 3D whole-body CE-MRA with a moderate amount of interaction, using a single MIP projection.

6.5 Paper VI: Objective Assessment of Vessel Geometry in 3D Whole-Body Contrast-Enhanced MRA

The danger of an acute event related to atherosclerosis is not well predicted by the classical "degree of stenosis" approach, which consists in identifying the highly stenosed vessels and measuring the luminal diameter reduction. The "arterial remodeling" model focuses on how vessel geometry and its changes during the course of atherogenesis influence blood flow patterns. Plaque vulnerability is related to wall shear stress, itself related to vessel tortuosity.

In this paper, we suggest two objective measures of vessel geometry, computed from whole-body contrast-enhanced MR angiograms. As in paper V, MIP are used as an interface with the 3D volume, to place a series of landmarks inside the main arteries. These landmarks constitute the node of a graph model of the arterial tree. They convey topological and anatomical information, as they separate the whole tree into segments, in a way similar to the analysis usually done in clinical practice. A cost function is built from the image data by computing the response of a vesselness filter for a predefined set of scales. Fast marching is then applied in 4D (three spatial dimensions and scale) to find the shortest path, within the arteries, between the landmarks. The suggested algorithm is able to handle the anisotropic character of the 4D hypervolume.Curvature and torsion are then computed using well-posed differentiation, based on Gaussian scale-space theory. Curvature is a measure of the rate at which the direction of the local tangent changes, whereas torsion measures the vessel's planarity. They are both needed to describe the 3D nature of the 3D curve.

The values of curvature and torsion along the vessel centreline are displayed on a surface rendering of the arterial tree, together with "curvature indexes" and "torsion indexes", which summarize the measurements by segment and for the whole tree.

In conclusion, we showed that it is possible to measure objectively and without segmentation the geometry of main arteries in whole-body CE-MRA.

References

[1] North American Symptomatic Carotid Endarterectomy Trial. Methods, patient characteristics, and progress. *Stroke*, 22(6):711–20 (1991).

[2] Randomised trial of endarterectomy for recently symptomatic carotid stenosis: final results of the MRC European Carotid Surgery Trial (ECST). *Lancet*, 351(9113):1379–87 (1998).

[3] Wikipedia, open-content encyclopedia. `http://en.wikipedia.org/wiki/Main_Page` (2004).

[4] Adalsteinsson D. and Sethian J. A Fast Level Set Method for Propagating Interfaces. *Journal of Computational Physics*, 118:269–277 (1995).

[5] Anderson C.M., Lee R.E., Levin D.L., de la Torre Alonso S., and D. S. Measurement of internal carotid artery stenosis from source MR angiograms. *Radiology*, 193(1):219–226 (1994).

[6] Aronsson M. *On 3D fibre measurements of digitized paper*. Ph.D. thesis, Swedish University of Agricultural Sciences (2002).

[7] Aylward S., Pizer S., Bullitt E., and Eberly D. Intensity ridge and widths for tubular object segmentation and description. In *IEEE Workshop on Mathematical Methods in Biomedical Image Analysis*, pages 131–138 (1996).

[8] Aylward S.R. and Bullitt E. Initialization, noise, singularities, and scale in height ridge traversal for tubular objects centerline extraction. *IEEE Transactions on Medical Imaging*, 21(2):61–75 (2002).

[9] Baskaran V., Pereles S., Nemcek Jr A.A., et al. Gadolinium-enhanced 3D MR angiography of renal artery stenosis: a pilot comparison of maximum intensity projection, multiplanar reformatting, and 3D volume-rendering postprocessing algorithms. *Academic Radiology*, 9(1):50–59 (2002).

[10] Beers M.H. and Berkow R., editors. *The Merck Manual of Diagnosis and Therapy*. Medical Services, USMEDSA, USHH (2004).

[11] Beutel J., Kundel H.L., and Van Metter R.L. *Handbook of Medical Imaging - Volume I. Physics and psychophysics*. SPIE Press (2000).

[12] Blankenhorn D.H., Brooks S.H., Selzer R.H., Crawford D.W., and Chin H.P. Assessment of atherosclerosis from angiographic images. *Proceedings of the Society for Experimental Biology and Medicine*, 145:1298–1300 (1974).

[13] Bloch F., Hanson W.W., and Packard M. Nuclear induction. *Physical Review*, 69(1):127 (1946).

[14] Bock M., Schoenberg S.O., Flömer F., Knopp M.V., and Schad L.R. Artery and vein separation in time-resolved MRA with correlation

analysis. In *XI International Workshop on Magnetic Resonance Angiography*, volume 41 of *Acta Radiologica Supplementum*, pages 64–65 (2000).

[15] Borgefors G. Distance Transformations in Digital Images. *Computer Vision, Graphics, and Image Processing*, 14(3):344–371 (1986).

[16] Borgefors G. On digital distance transforms in three dimensions. *Computer Vision and Image Understanding*, 64(3):368–376 (1996).

[17] Brown B.G., Bolson E.L., and Dodge H.T. Dynamic mechanisms in human coronary stenosis. *Circulation*, 70(6):917–922 (1984).

[18] Buckheit J. and Donoho D.L. Wavelab and reproducible research. In A. Antoniadis, editor, *Wavelets and Statistics*. Springer-Verlag, Berlin, New York. (1995).

[19] Bühler K., Felkel P., and La Cruz A. Geometric methods for vessel visualization and quantification - a survey. In G. Brunett, B. Hamann, H. Müller, and L. Linsen, editors, *Geometric Modelling for Scientific Visualization*, pages 399–420. Springer-Verlag (2004).

[20] Carriero A., Maggialetti A., Pinto D., et al. Contrast-Enhanced Magnetic Resonance Angiography MoBI-Trak in the Study of Peripheral Vascular Disease. In *CardioVascular and Interventional Radiology*, volume 25, pages 42–47. Springer-Verlag, New York (2002).

[21] Chakeres D.W., Schmalbrock P., Brogan M., Yuan C., and Cohen L. Normal venous anatomy of the brain: demonstration with gadopentetate dimeglumine in enhanced 3-D MR angiography. *American Journal of Roentgenology*, 156(1):161–172 (1991).

[22] Chapman N., Witt N., Gao X., et al. Computer algorithms for the automated measurement of retinal arteriolar diameters. *British Journal of Ophthalmology*, 85(1):74–9 (2001).

[23] Coeurjolly D. and Klette R. A Comparative Evaluation of Length Estimators of Digital Curves. *IEEE Transactions on Pattern Analysis and Machine Intelligence*, 26(2):252–258 (2004).

[24] Coeurjolly D. and Svensson S. Estimation of Curvature along Curves with Application to Fibres in 3D Images of Paper. In J. Bigun and T. Gustavsson, editors, *SCIA*, volume 2749 of *Lecture Notes in Computer Science*, pages 247–254. Springer-Verlag, Berlin Heidelberg (2003).

[25] Cohen L.D. and Kimmel R. Global minimum for active contour models: a minimal path approach. *International Journal of Computer Vision*, 24(1):57–78 (1997).

[26] Cormen T.H., Leiserson C.E., and Rivest R.L. *Introduction to algorithms*. McGraw-Hill (1998).

[27] Couprie M., Nivando Bezerra F., and Bertrand G. Topological oper-

ators for grayscale image processing. *Journal of Electronic Imaging*, 10(4):1003–1015 (2001).

[28] Creasy J.L., Price R.R., Presbrey T., Goins D., Partain C.L., and Kessler R.M. Gadolinium-enhanced MR angiography. *Radiology*, 175(1):280–283 (1990).

[29] Damadian R. Tumor Detection by Nuclear Magnetic Resonance. *Science*, 171(976):1151–1153 (1971).

[30] Danielsson P.E. Euclidean distance mapping. *Computer Graphics and Image Processing*, 14(3):227–248 (1980).

[31] Dellepiane S.G. and Fontana F. Extraction of intensity connectedness for image processing. *Pattern Recognition Letters*, 16(3):313–324 (1995).

[32] Dellepiane S.G., Fontana F., and Vernazza G.L. Nonlinear image labelling for multivalued segmentation. *IEEE Transactions on Image Processing*, 5(3):429–446 (1996).

[33] den Boer J.A. and Hoogeveen R. Contrast enhanced MR angiography. *Medica Mundi*, 45(1):10–22 (2001).

[34] Deschamps T. *Extraction de courbes et surfaces par méthodes de chemins minimaux et ensemble de niveaux. Applications en imagerie médicale 3D*. Ph.D. thesis, Université de Paris - Dauphine (2001). In english.

[35] Descoteaux M., Collins L., and Siddiqi K. A Multi-Scale Geometric Flow for Segmenting Vasculature in MRI. In *Computer Vision Approaches to Medical Image Analysis (CVAMIA)*. Springer-Verlag, Prague (2004).

[36] Dijkstra E.W. A note on two problems in connexion with graphs. *Numerische Mathematik*, 1:269–271 (1959).

[37] Eberly D., Gardner R., Morse B., Pizer S., and Scharlah C. Ridges for image analysis. *Journal of Mathematical Imaging and Vision*, 4(4):353–373 (1994). ISSN 0924-9907.

[38] Farr R.F. and Allisy-Roberts P.J. *Physics for medical imaging*. Saunders (1998).

[39] Fayad Z.A., Sirol M., Nikolaou K., Choudhury R.P., and Fuster V. Magnetic resonance imaging and computed tomography in assessment of atherosclerotic plaque. *Current Atherosclerosis Reports*, 6(3):323–242 (2004).

[40] Felkel P. Segmentation of vessels in peripheral CTA datasets. Technical report, VRVis: Zentrum für Virtual Reality und Visualisierung Forschungs (2001).

[41] Ferrari A.U., Radaelli A., and Centola M. Invited review: aging and the cardiovascular system. *Journal of Applied Physiology*,

95(6):2591–2597 (2003).

[42] Florack L.M.J. *Image structure*. Kluwer Academic Publishers (1997).

[43] Florack L.M.J. Mathematical techniques for image analysis (2003). Lecture Notes.

[44] Florack L.M.J., Ter Haar Romeny B.M., Koenderink J.J., and Viergever M. Scale and the differential structure of images. *Image and Vision Computing*, 10(6):376–388 (1992).

[45] Frangi A.F., Niessen W.J., Hoogeveen R.M., van Walsum T., and Viergever M.A. Model-based quantitation of 3-D magnetic resonance angiographic images. *IEEE Transactions on Medical Imaging*, 18(10):946–956 (1999).

[46] Frangi A.F., Niessen W.J., Nederkoorn P.J., Bakker J., Mali W.P., and Viergever M.A. Quantitative analysis of vascular morphology from 3D MR angiograms: In vitro and in vivo results. *Magnetic Resonance in Medecine*, 45(2):311–22 (2001).

[47] Frangi A.F., Niessen W.J., Nederkoorn P.J., Elgersma O.E.H., and Viergever M.A. Three-dimensional model-based stenosis quantification of the carotid arteries from contrast-enhanced MR angiography. In *Workshop on Mathematical methods in Biomedical Image Analysis*, pages 110–118 (2000).

[48] Frangi A.F., Niessen W.J., Vincken K.L., and Viergever M.A. Multiscale vessel enhancement filtering. In *Medical Image Computing and Computer-Assisted Intervention - MICCAI '98*, pages 130–137. Springer Verlag (1998).

[49] Glagov S., Weisenber E., Zarins C.K., Stankunavicius R., and Kolettis G.J. Compensatory enlargement of human atherosclerotic coronary arteries. *New England Journal of Medicine*, 316(22):1371–1375 (1987).

[50] Gonzalez R.C. and Woods R.E. *Digital Image Processing*. Prentice Hall (2001).

[51] Gorman C. and Park A. The Fires Within. *Time Magazine* (2003).

[52] Goyen M., Herborn C.U., Kröger K., Lauenstein T.C., Debatin J.F., and Ruehm S.G. Detection of atherosclerosis: systemic imaging for systemic disease with whole whole-body three-dimensional MR angiography-initial experience. *Radiology*, 227(1):277–282 (2003).

[53] Griffin L.D. and Colchester A.C.F. Superficial and deep structure in linear diffusion scale space: isophotes, critical points and separatrices. *Image and Vision Computing*, 13(7):543–557 (1995).

[54] Haacke M.E., Brown R.W., Thompson M.R., and R. V. *Magnetic Resonance Imaging: Physical Principles and Sequence Design*. John Wiley and Sons (1999).

[55] Hanke H., Lenz C., and Finking G. The discovery of the pathophysiological aspects of atherosclerosis–a review. *Acta Chirurgica Belgica*, 101(4):162–169 (2001).

[56] Hascheck E. Lindenthal O.T. Ein Beitrag zur praktischen verwethung der photographie nach Röntgen. *Wiener klinische wochenschrift*, 9(4):63–64 (1896).

[57] Hernandez M., Barrena R., Hernandez G., Sapiro G., and Frangi A.F. Pre-clinical evaluation of implicit deformable models for three-dimensional segmentation of brain aneurysms in CTA. In *SPIE Medical Imaging 2003 Symposium*, volume 5032, page 139 (2003).

[58] Hladuvka J., König A., and Gröller E. Exploiting eigenvalues of the hessian matrix for volume decimation. In *9th International Conference in Central Europe on Computer Graphics, Visualization, and Computer Vision*, pages 124–129 (2001).

[59] Hoffmann K.R., Nazareth D.P., Miskolczi L., et al. Vessel size measurements in angiograms: a comparison of techniques. *Medical Physics*, 29(7):1622–1633 (2002).

[60] Hoogeveen R.M., Bakker C.J., and Viergever M.A. Limits to the accuracy of vessel diameter measurement in MR angiography. *Journal of Magnetic Resonance Imaging*, 8(6):1228–1235 (1998).

[61] Imielinska C., Metaxas D.N., Udupa J.K., Jina Y., and Chen T. Hybrid Segmentation of Anatomical Data. In W.J. Niessen and M.A. Viergever, editors, *MICCAI*, volume 2208 of *Lecture Notes in Computer Science*, pages 1048–1057. Springer (2001). ISBN 3-540-42697-3.

[62] Johansson L., Lundberg A., Erriksson M.L., Hoogeveen R.M., and Ahlström H. Whole body contrast enhanced magnetic resonance angiography. A tool for screening and evaluation of total plaque burden? In *ISMRM Eleventh Meeting Proceedings* (2003).

[63] Kanitsar A. *Advanced Visualization Techniques for Vessel Investigation*. Master's thesis, University of Technology Vienna, Institute of Computergraphics and Algorithm (2001).
URL `http://www.cg.tuwien.ac.at/research/vis/angiovis/`

[64] Kanitsar A., Fleischmann D., Wegenkittl R., Felkel P., and Gröller M.E. CPR - Curved Planar Reformation. In *13th IEEE Visualization 2002 Conference (VIS 2002)*, pages 37–44 (2002).

[65] Kanitsar A., Wegenkittl R., Fleischmann D., and Gröller M.E. Advanced Curved Planar Reformation: Flattening of Vascular Structures. In *IEEE Visualization 2003*, pages 43–50 (2003).
URL `http://www.cg.tuwien.ac.at/research/vis/`

`adapt/`

[66] Kaufman A. Volume Visualization: principles and advances. Course notes 24, SIGGRAPH (1998).

[67] Kellar K.E., Fujii D.K., Gunther W.H., Briley-Saebø K., Spiller M., and Koenig S.H. NC100150, a preparation of iron oxide nanoparticles ideal for positive-contrast angiography. *MAGMA*, 8(3):207–13 (1999).

[68] Kerwin W., Han C., Chu B., et al. A quantitative vascular analysis system for evaluation of atherosclerotic lesions by MRI. In *MICCAI 2001*, pages 786–794. Springer Verlag (2001).

[69] Kiechl S. and Willeit J. The natural course of atherosclerosis. Part II: vascular remodeling. Bruneck Study Group. *Arteriosclerosis,Thrombosis, and Vascular Biology Thromb Vasc Biol*, 19(6):1491–1498 (1999).

[70] Kim Y. and Horii S.C. *Handbook of Medical Imaging - Volume 3. Display and PACS.* SPIE Press (2000).

[71] Kimmel R. and Sethian J.A. Optimal Algorithm for Shape from Shading and Path Planning. *Journal of Mathematical Imaging and Vision*, 14(3):237–244 (2001).

[72] Kindlmann G., Whitaker R., Tasdizen T., and Möller T. Curvature-Based Transfer Functions for Direct Volume Rendering: Methods and Applications. In *IEEE Visualization 2003 Conference (VIS 2003)*, pages 513–520 (2003).

[73] Koenderink J.J. and van Doorn A.J. The structure of images. *Biological Cybernetics*, 50:363–370 (1984).

[74] Koenderink J.J. and van Doorn A.J. Local features of smooth shapes: ridges and courses. In B.C. Vemuri, editor, *Geometric Methods in Computer Vision II*, volume 2031, pages 2–13. SPIE (1993).

[75] Koller T.M., Gerig G., Székely G., and Dettwiller D. Multiscale detection of curvilinear structures in 2-D and 3-D image data. In *5th Intrenational Conference on Computer Vision*, pages 864–869 (1995).

[76] Kouwenhoven M., Bakker C.J., Hartkamp M., and Mali W.P.T.M. *Vascular diagnostics*, chapter Current MR Angiographic Imaging Techniques, a survey, pages 375–400. Springer Verlag (1994).

[77] Krissian K., Malandain G., and Ayache N. Model based multiscale detection and reconstruction of 3D vessels. Technical report, INRIA (1998).

[78] Krissian K., Malandain G., Ayache N., Vaillant R., and Trousset Y. Model-based detection of tubular structures in 3D images. *Computer Vision and Image Understanding*, 80(2):130–171 (2000).

[79] Kruger R.A., Mistretta C.A., Lancaster J., et al. A digital video image

processor for real-time x-ray subtrac-tion imaging. *Optical Engineering*, 17(6):652–657 (1978).

[80] Kumar N., Welti D., and Ernst R.R. NMR-Fourier-Zeugmatography. *Journal of Magnetic Resonance*, 18(1):69–83 (1975).

[81] Langlois S., Desvignes M., Constans J.M., and Revenu M. MRI geometric distortion: a simple approach to correcting the effects of non-linear gradient fields. *Journal of Magnetic Resonance Imaging*, 9(6):821–831 (1999).

[82] Lauffer R., Parmelee D., Dunham S., et al. MS-325: albumin-targeted contrast agent for MR angiography. *Radiographics*, 207(2):1529–538 (1998).

[83] Lauterbur P.C. Image formation by induced local interactions: examples of employing nuclear magnetic resonance. *Nature*, 242(5394):190–191 (1973).

[84] Lei T.H., Udupa J.K., Saha P.K., and Odhner D. Artery-vein separation via MRA - An image processing approach. *IEEE Transactions on Medical Imaging*, 20(8):689–703 (2001).

[85] Leiner T., De Vries M., Hoogeven R., Vasbinder G.B.C., Lemaire E., and Van Engelshoven J. Contrast-enhanced peripheral MR angiography at 3.0 Tesla: initial experience with a whole-body scanner in healthy volunteers. *Journal of Magnetic Resonance and Imaging*, 17(5):609–614 (2003).

[86] Léoni J. *Physiopathologie de l'athérosclérose - Mécanismes et prévention de l'athérothrombose*. Ph.D. thesis, Faculté de Médecine et de Pharmacie de Besançon (2001).

[87] Libby P. Atherosclerosis: the new view. *Scientific American*, pages 47–55 (2002).

[88] Lillholm M. and Pedersen K.S. Jet Based Feature Classification (2004). In Proceedings of International Conference on Pattern Recognition, Cambridge, United Kingdom. August 2004.

[89] Lin Q. *Enhancement, extraction, and visualization of 3D volume data*. Ph.D. thesis, Computer Vision Laboratory, Linköping University (2003).

[90] Lin W., Haacke E.M., Smith A.S., and Clampitt M.E. Gadolinium-enhanced high-resolution MR angiography with adaptive vessel tracking: preliminary results in the intracranial circulation. *Journal of Magnetic Resonance Imaging*, 2(3):277–284 (1992).

[91] Lindeberg T. Effective scale: a natural unit for measuring scale-space lifetime. *IEEE Transactions on Pattern Analysis and Machine Intelligence*, 15(10):1068–1074 (1993).

[92] Lindeberg T. *Scale-Space Theory in Computer Vision*. Kluwer Acad-

emic Publisher (1994).

[93] Lindeberg T. Edge Detection and Ridge Detection with Automatic Scale Selection. *International Journal of Computer Vision*, 30(2):117–156 (1998).

[94] Lindeberg T. Principles for automatic scale selection. *Handbook on computer vision and applications*, 2:239–274 (1999).

[95] Lopez A.M., Lloret D., Serrat J., and Villanueva J. Multilocal creaseness on the level-set extrinsic curvature. *Computer Vision and Image Understanding*, 77:111–144 (2000).

[96] Lopez A.M., Lumbreras F., Serrat J., and Villanueva J. Evaluation of methods for ridge and valley detection. *IEEE Transactions on Pattern Analysis and Machine Intelligence*, 21(4):327–335 (1999).

[97] Lorensen W.E. and Cline H.E. Marching Cubes: A High Resolution 3D Surface Construction Algorithm. In *Computer Graphics (Proceedings of SIGGRAPH '87)*, volume 21, pages 163–169 (1987).

[98] Lorenz C., Carlsen I.C., Buzug T.M., Fassnacht C., and Weese J. Multi-scale line segmentation with automatic estimation of width, contrast and tangential direction in 2D and 3D medical images. In *CVRMed-MRCAS'97*, Lecture Notes in Computer Science, pages 233–242 (1997).

[99] Maas R. and Boger R.H. Old and new cardiovascular risk factors: from unresolved issues to new opportunities. *Atherosclerosis Supplement*, 4(4):5–17 (2003).

[100] Mansfield P. Multi-Planar Image Formation Using NMR Spin Echoes. *Journal Of Physics C-Solid State Physics*, 10(3):55–58 (1977).

[101] Marchal G., Bosmans H., Van Hecke P., Jiang Y.B., Aerts P., and Bauer H. Experimental Gd-DTPA polylysine enhanced MR angiography: sequence optimization. *Journal of Computed Assisted Tomography*, 15(4):711–715 (1991).

[102] Marieb E.M. *Human anatomy and physiology*. The Benjamin-Cummings Publishing Company (1995).

[103] Martel A.L., Fraser D., Delay G.S., Morgan P.S., and Moody A.R. Separating arterial and venous components from 3D dynamic contrast-enhanced MRI studies using factor analysis. *Magnetic Resonance in Medecine*, 49(5):928–933 (2003).

[104] Mauch S. *Efficient Algorithms for Solving Static Hamilton-Jacobi Equations*. Ph.D. thesis, California Institute of Technology, Pasadena, California (2003).

[105] Meijering E.H.W., Niessen W., and Viergever M.A. Quantitative evaluation of convolution-based methods for medical image interpolation. *Medical Image Analysis*, 5(2):111–126 (2001).

[106] Mistretta C.A. Relative characteristics of MR angiography and competing vascular imaging modalities. *Journal of Magnetic Resonance Imaging*, 3(5):685–698 (1993).

[107] Morse B.S., Pizer S., and Liu A. Multiscale medial analysis of medical images. *Image and Vision Computing*, 12(6):327338 (1994).

[108] Mroz L. and Hauser H. Interactive High-Quality Maximum Intensity Projection. In M. Gross and F.R.A. Hopgood, editors, *EUROGRAPHICS Š2000*, volume 19 (2000).

[109] Nilsson S., Berglund I., Bylund H., et al. Quantitation of atherosclerosis in femoral arteriography with ECG gated exposures. *Acta Radiologica*, 29:311–315 (1988).

[110] Nowak R. Wavelet-based rician noise removal for magnetic resonance imaging. *IEEE Transactions on Image Processing*, 8(10):1408–1419 (1999).

[111] Nyström I. and Smedby O. Skeletonization of volumetric vascular images – Distance information utilized for visualization. *Journal of Combinatorial Optimization*, 5(1):27–41 (2001). Special Issue on Optimization Problems in Medical Applications.

[112] Nyul L.G., Falcao A., and Udupa J.K. Fuzzy-connected 3D image segmentation at interactive speeds. *Graphical Models*, 64(5):259–281 (2002).

[113] Nyul L.G., Udupa J.K., and Saha P.K. Incorporating a measure of local scale in voxel-based 3-D image registration. *IEEE Transactions on Medical Imaging*, 22(2):228–37 (2003).

[114] Olsson A.G., Carlson L.A., Erikson U., Helmius G., Hemmingsson A., and Ruhn G. Regression of computer estimated femoral atherosclerosis after pronounced serum lipid lowering in patients with asymptomatic hyperlipidaemia. *Lancet*, 1(8284):1311 (1982).

[115] Osher S. and Sethian J.A. Fronts Propagating With Curvature-Dependent Speed - Algorithms Based On Hamilton-Jacobi Formulations. *Journal of Computational Physics*, 79(1):12–49 (1988).

[116] Pasterkamp G., Schoneveld A.H., van der Wal A.C., et al. Relation of arterial geometry to luminal narrowing and histologic markers for plaque vulnerability: the remodeling paradox. *Journal of the American College of Cardiology*, 32(3):655–662 (1998).

[117] Pelletier D., Garrison K., and Henry R. Measurement of whole-brain atrophy in multiple sclerosis. *Journal of Neuroimaging*, 14(3):11–19 (2004).

[118] Pizer S.M., Burbeck C.A., Coggins J.M., Fritsch D.S., and Morse B.S. Object shape before boundary shape: Scale-space medial axes. *Journal of Mathematical Imaging and Vision*, 4:303–313 (1994).

[119] Poli A., Tremoli E., and Colombo A. Ultrasonographic measurement of the common carotid artery wall thickness in hypercholesterolemic patients: a new model for the quantitation and follow-up of preclinical atherosclerosis in living human subjects. *Atherosclerosis*, 70:253–261 (1988).

[120] Press W.H., Flannery B.P., Teukolsky S.A., and Vetterling W.T. *Numerical Recipes: The Art of Scientific Computing*. Cambridge University Press, Cambridge (UK) and New York, 2nd edition (1992). ISBN 0-521-43064-X.

[121] Prince M., Grist T.M., and Debatin J.F. *3D contrast MR angiography*. Springer (1999).

[122] Prokesch R.W., Coulam C.H., Chow L.C., Bammer R., and Rubin G.D. CT angiography of the subclavian artery: utility of curved planar reformations. *Journal of Computer Assisted Tomography*, 26(2):199–201 (2002).

[123] Purcell E., Torrey H., and Pound R. Resonance absorption by nuclear magnetic moments in a solid. *Physical review*, 69:37–38 (1946).

[124] Quick H.H., Debatin J.F., and Ladd M.E. MR imaging of the vessel wall. *European Radiology*, 12(4):889–900 (2002).

[125] Rasband W. ImageJ. `http://rsb.info.nih.gov/ij/` (1997). National Institutes of Health, Bethesda, Maryland, USA.

[126] Reddy K. and Yusuf S. Emerging epidemic of cardiovascular disease in developing countries. *Circulation*, 97:596–601 (1998).

[127] Rinck P.A. *Magnetic Resonance in Medicine - The basic textbook of the european magnetic resonance forum*. Blackwell scientific publications (1993).

[128] Rosenfeld A. Fuzzy Digital Topology. *Information and Control*, 40:76–87 (1979).

[129] Rosenfeld A. On connectivity properties of grayscale pictures. *Pattern Recognition*, 16(1):47–50 (1983).

[130] Ruehm S.G., Goyen M., Barkhausen J., et al. Rapid magnetic resonance angiography for detection of atherosclerosis. *Lancet*, 357(9262):1086–1091 (2001).

[131] Ruhn G., Erikson U., Helmius G., and Hemmingsson A. Computerized quantitation of atherosclerosis in an experimental model. Arteriography and microdensitometry. *Acta Radiologica Diagnostica*, 23(6):621–624 (1982).

[132] Saha P.K., Udupa J.K., and Odhner D. Scale-based fuzzy connected image segmentation: theory, algorithms, and validation. *Computer Vision and Image Understanding*, 77(2):145–174 (2000).

[133] Sato Y., Nakajima S., Shiraga N., et al. Three-dimensional multi-scale

line filter for segmentation and visualization of curvilinear structures in medical images. *Medical Image Analysis*, 2(2):143–168 (1998).

[134] Sato Y., Shiraga N., Nakajima S., Tamura S., and Kikinis R. Local Maximum Intensity Projection (LMIP): A New Rendering Method for Vascular Visualization. *Journal of Computer Assisted Tomography*, 22(6):912–917 (1998).

[135] Sato Y., Tanaka H., Nishii T., et al. Limits on the accuracy of 3-D thickness measurement in magnetic resonance images–effects of voxel anisotropy. *IEEE Transactions on Medical Imaging*, 22(9):1076–88 (2003).

[136] Sato Y., Westin C., Bhalerao A., et al. Tissue classification based on 3D local intensity structures for volume rendering. *IEEE Transactions on visualization and computer graphics*, 6(2):160–180 (2000).

[137] Schreiner S., Dawant B.M., Paschal C.B., and Galloway R.L. The importance of ray pathlengths when measuring objects in maximum intensity projection images. *IEEE Transactions on Medical Imaging*, 15(4):568–579 (1996).

[138] Sethian J. A fast marching level set method for monotonically advancing fronts. *Proceedings of the Natural Academy of Sciences*, 93(4):1591–1595 (1996).

[139] Sethian J. Fast marching methods. *SIAM Review*, 41(2):199–235 (1999).

[140] Sethian J. *Level set methods and fast marching methods*. Cambridge University Press (1999).

[141] Seymour H.R., Matson M.B., Belli A.M., Morgan R., Kyriou J., and Patel U. Rotational digital subtraction angiography of the renal arteries: technique and evaluation in the study of native and transplant renal arteries. *British Journal of Radiology*, 74(878):134–141 (2001).

[142] Shapiro L. and Stockman C. *Computer Vision*, chapter Region Growing, pages 289–291. Prentice Hall (2001).

[143] Sijbers J., den Dekker A.J., Van der Linden A., Verhoye T.M., and Van Dyck D. Adaptive anisotropic noise filtering for magnitude MR data. *Magnetic Resonance Imaging*, 17(10):1533–1539 (1999).

[144] Silvela J. and Portillo J. Breadth-first search and its application to image processing problems. *IEEE Transactions on Image Processing*, 10(8):1194–1199 (2001).

[145] Smedby O. *Angiographic methods for the study of fluid mechanical factors in atherogenesis*. Ph.D. thesis, Department of Diagnostic Radiology, Uppsala University (1992).

[146] Smedby O. Do plaques grow upstream or downstream?: an angiographic study in the femoral artery. *Arteriosclerosis,Thrombosis, and*

Vascular Biology, 17(5):912–918 (1997).

[147] Smedby O. and Bergstrand L. Tortuosity and atherosclerosis in the femoral artery: what is cause and what is effect? *Annals of Biomedical Engineering*, 24(4):474–480 (1996).

[148] Stary H.C., Chandler A.B., Glagov S., et al. A definition of initial, fatty streak, and intermediate lesions of atherosclerosis. A report from the Committee on Vascular Lesions of the Council on Arteriosclerosis, American Heart Association. *Circulation*, 89(5):2462–2478 (1994).

[149] Stevenson D., Smith L., and Robinson G. Working towards the automatic detection of blood vessels in X-ray angiograms. *Pattern Recognition Letters*, 6(2):107–112 (1987).

[150] Störk S., Van Den Beld A.W., Von Schacky C., et al. Carotid Artery Plaque Burden, Stiffness, and Mortality Risk in Elderly Men: A Prospective, Population-Based Cohort Study. *Circulation*, 110(3):344–348 (2004).

[151] Stroud J.S., Berger S., and Saloner D. Influence of stenosis morphology on flow through severely stenotic vessels: implications for plaque rupture. *Journal of Biomechanics*, 33(4):443–455 (2000).

[152] Sun Y. and Parker D.L. Performance Analysis of Maximum Intensity Projection Algorithm for Display of MRA Images. *IEEE Transactions on Medical Imaging*, 18(12):1154–1169 (1999).

[153] Suri J., Liu K., Reden L., and Laxminarayan S. A review on MR vascular image processing algorithms: acquisition and prefiltering: Part I. *IEEE Transactions on information technology in biomedicine*, 6(4):324–337 (2002).

[154] Suri J., Liu K., Reden L., and Laxminarayan S. A review on MR vascular image processing algorithms: skeleton versus non skeleton approaches: Part II. *IEEE Transactions on Information Technology in Biomedicine*, 6(4):338–350 (2002).

[155] ter Haar Romeny B.M. *Front-End Vision and Multi-Scale Image Analysis*. Kluwer Academic Publisher (2003).

[156] Tsai Y.R., Cheng L., Osher S., and Zhao H. Fast sweeping algorithms for a class of Hamilton-Jacobi equations. *SIAM Journal on Numerical Analysis*, 41(2):673–694 (2003).

[157] Tsitsiklis J.N. Efficient algorithms for globally optimal trajectories. *IEEE Transactions on Automatic Control*, 40(9):1528–1538 (1995).

[158] Udupa J.K. and Samarasekera S. Fuzzy connectdness and object definition: theory, algorithms, and applications in image segmentation. *Graphical Models and Image Processing*, 58(3):246–261 (1996).

[159] Udupa J.K., Wei L., Samarasekera S., Miki Y., van Buchem M.A., and Grossman R.I. Multiple Sclerosis Lesion Quantification Using Fuzzy-

Connectedness Principles. *IEEE Transactions on Medical Imaging*, 16(5):598–609 (1997).

[160] van Bemmel C., Spreeuwers L., Viergever M., and Niessen W. Level-Set Based Carotid Artery Segmentation for Stenosis Grading. In *MICCAI 2002*, pages 36–43. Springer Verlag (2002).

[161] van Bemmel C., Spreeuwers L., Viergever M., and Niessen W. Level-set-based artery-vein separation in blood pool agent CE-MR angiograms. *IEEE Transactions on Medical Imaging*, 22(10):1224–1234 (2003).

[162] van Bemmel C.M., Wink O., Verdonck B., Viergever M., and Niessen W.J. Blood Pool contrast-enhanced MRA: improved arterial visualization in the steady state. *IEEE Transactions on Medical Imaging*, 22(5):645–652 (2003).

[163] Walker M.F., Souza S.P., and Dumoulin C.L. Quantitative flow measurement in phase contrast MR angiography. *Journal of Computed Assisted Tomography*, 12(2):304–313 (1988).

[164] Wang B., Saha P.K., Udupa J.K., et al. 3D airway segmentation via hyperpolarized 3He gas MRI by using scale-based fuzzy connectedness. *Computerized Medical Imaging and Graphics*, 28(1-2):77–86 (2004).

[165] Wang D., Doddrell D.M., and Cowin G. A novel phantom and method for comprehensive 3-dimensional measurement and correction of geometric distortion in magnetic resonance imaging. *Magnetic Resonance Imaging*, 22(4):529–542 (2004).

[166] Ward M.R., Pasterkamp G., Yeung A.C., and Borst C. Arterial remodeling. Mechanisms and clinical implications. *Circulation*, 102(10):1186–1191 (2000).

[167] Wehrli F., Shimakawa A., Gullberg G.T., and MacFall J.R. Time-of-flight MR flow imaging: selective saturation recovery with gradient refocusing. *Radiology*, 160(3):781–785 (1986).

[168] Wenwang Z. The fast sweeping method of eikonal equations and its parallelism. Technical report, KTH Numerical analysis and computer science (2003).

[169] Westenberg J.J.M., van der Geest R., Wasser M., et al. Vessel diameter measurements in gadolinium contrast enhanced three dimensional MRA of peripheral arteries. *Magnetic Resonance Imaging*, 18(1):13–22 (2000).

[170] Wikström J., Johansson L., Ericsson A., Børseth A., Åkeson P., and Ahlström H. Abdominal vessel enhancement with the blood pool agent NC100150: relation to dose and echo time. In *ISMRM Proceedings*, abstract no. 1046. Sydney (1998).

[171] Wink O., Niessen W., and Viergever M. Multiscale vessel tracking. *IEEE Transactions on Medical Imaging*, 23(1):130–133 (2004).

[172] Witkin A.P. Scale-space filtering. In *Proceedings of the 7th International Joint Conference on Artificial Intelligence*, pages 1019–1022 (1983).

[173] Yim P.J., Mullick R., Summers R.M., et al. Measurement of stenosis from magnetic resonance angiography using vessels skeletons. In *SPIE Medical Imaging* (2000).

[174] Young N., Pekar V., and Weese J. Vessel Segmentation for Visualization of MRA with Blood Pool Contrast Agent. In *MICCAI 2001*, pages 491–498. Springer Verlag (2001).

[175] Yu Z. and Bajaj C. A Segmentation-Free Approach for Skeletonization of Gray-Scale Images via Anisotropic Vector Diffusion. In *Proceedings of 2004 IEEE International Conference on Computer Vision and Pattern Recognition (CVPR'04)*, volume 1, pages 415–420. Washington, DC (2004).

[176] Zir M., Miller S.W., Dinsmore R.E., Gilbert J.P., and Harthorne J.W. Interobserver variability in coronary angiography. *Circulation*, 53:627–632 (1976).

[177] Zucker S.W. Region Growing: childhood and adolescence. *Computer Graphics and Image processing*, 5:382–399 (1976).

[178] Zuiderveld K.J., Koning A., and Viergever M.A. Techniques for speeding up high-quality perspective Maximum Intensity Projection. *Pattern Recognition Letters*, 15(5):507–517 (1994).

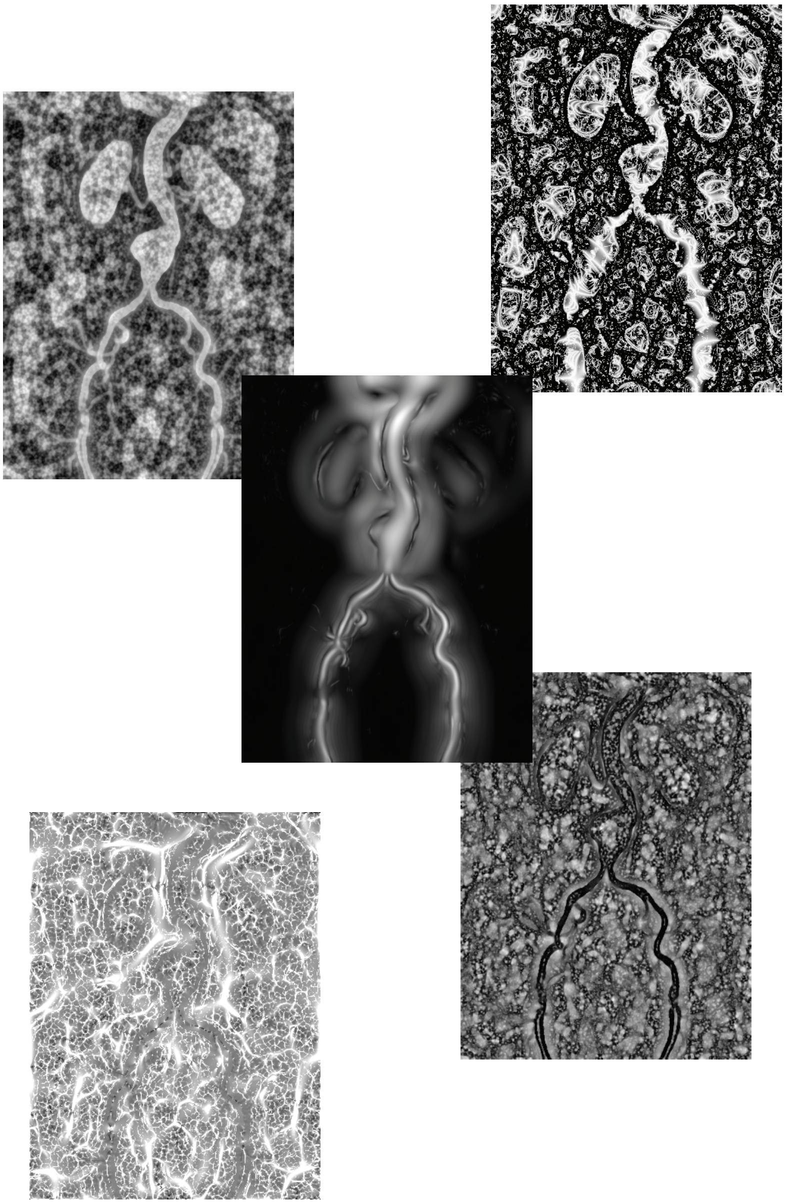

Acknowledgements

This thesis summarizes research projects carried out at the Centre for Image Analysis and Uppsala University Hospital between June 1999 and September 2004. I would like here to express my gratitude to the people who made it all possible.

My supervisor, Professor Gunilla Borgefors. From the very first day we met, in Paris in early 1999, you did everything to make me feel welcome. You always kept an open mind about my scientific choices, even if the paths I chose sometimes wandered away from your footsteps. Thank you for your constant support, and for allowing me to pursue things in my own way.

My co-supervisor, Professor Örjan Smedby. I have learned a lot from you and your unique double competence. I will try to always keep in mind that one of the most important aspects of cooperative research is to understand each other's language.

My second co-supervisor, Doctor Hans Frimmel, for helping me squeeze the bitter-sweet juice out of my writing. I hope our collaboration on the vessel geometry project will go on after this thesis is defended.

The VISIT program and the people who worked hard for me to skip bothering about money during these five years.

All my colleagues at CBA, past and present, for making it such a special place. Carolina for being the sweetest roommate; Stina for a very pleasant and intensive semester of teaching; Ida for her never-ending smile; Ingela for her competence and spirit: keep up the fight!; Lucia for her fantastic tiramisu recipe: it's mine now ☺; Nataša for a lot of fuzzy reasons; Joakim for lightening up the Monday seminars; Ola and Mats, the math brothers, for the scientific discussions; Bosse for having helped me improve my Swedish by talking so fast; and everybody that I did not mention here but do not forget. Good luck to you all. A very special thanks to Lena. You have always been there to help me with the oddities of the Swedish administration and my laziness to comply with the paperwork.

Special thanks go to my former flatmate Felix. You showed me that science was a matter of creativity, and I showed you that French cuisine also was! I am very grateful for the thorough review you did on this thesis. Good luck for the future for you and Jenni!

The people at the MR Department of Uppsala University Hospital. Lars, Rolf, Arvid, Joel, Jan, Lena, the boss Håkan, and all the clinical staff. Anders L. is especially acknowledged for spending time uploading tremendous amounts of data, packing up our hard disks with material to work on.

My principal co-authors on the papers included in this thesis: Adam Löfving, Erik Vidholm, Joel Kullberg, Qingfen Lin and Hans Frimmel. Thanks to you, I learned that research is much more fun as a cooperative process.

I came to Sweden in May 1999, on a Tuesday morning. The very same evening, I was playing boule at Odinslund, which I have done there and almost everywhere in Sweden many times since. I am endlessly grateful to Sven-Erick, Christina, Staffan, Erik, and Ingrid for this first evening. I also want to thank all the MoPSes, past and present, and all my fellow players in the small world of boulesverige, for making my Swedish years so enjoyable. I owe you a lot, and I'll try to come back from time to time to check if you can still cope with the French carreaux.

My friends from far-away France. Jérôme, Sylvain and Catherine, Thierry and Alix, Gilles and Patricia, Olivier, Nicolas and Karine. It is good to know you always are here, and I look forward to seeing you more often than every second year.

Ma famille à Sanxay et Sheffield : mes parents et ma soeur Virginie. Dans les bons et les moins bons moments, vous êtes toujours à mes côtés.

There is one person left to thank. Lots of things have happened during the past five years, and the most important is you, Liliana, becoming a part of my life. There would be so much to thank about, and not least the part you played in the writing and reviewing of this thesis. I love you with all my heart.

Uppsala, September 2004

Xavier